JCB Journal of Cell Biology

ARTICLE

# FIGNL1 associates with KIF1Bβ and BICD1 to restrict dynein transport velocity during axon navigation

Melody Atkins[1], Laïla Gasmi[1], Valérie Bercier[2], Céline Revenu[2], Filippo Del Bene[2], Jamilé Hazan[1], and Coralie Fassier[1]

**Neuronal connectivity relies on molecular motor-based axonal transport of diverse cargoes. Yet the precise players and regulatory mechanisms orchestrating such trafficking events remain largely unknown. We here report the ATPase Fignl1 as a novel regulator of bidirectional transport during axon navigation. Using a yeast two-hybrid screen and coimmunoprecipitation assays, we showed that Fignl1 binds the kinesin Kif1bβ and the dynein/dynactin adaptor Bicaudal D-1 (Bicd1) in a molecular complex including the dynactin subunit dynactin 1. Fignl1 colocalized with Kif1bβ and showed bidirectional mobility in zebrafish axons. Notably, Kif1bβ and Fignl1 loss of function similarly altered zebrafish motor axon pathfinding and increased dynein-based transport velocity of Rab3 vesicles in these navigating axons, pinpointing Fignl1/Kif1bβ as a dynein speed limiter complex. Accordingly, disrupting dynein/dynactin activity or Bicd1/Fignl1 interaction induced motor axon pathfinding defects characteristic of Fignl1 gain or loss of function, respectively. Finally, pharmacological inhibition of dynein activity partially rescued the axon pathfinding defects of Fignl1-depleted larvae. Together, our results identify Fignl1 as a key dynein regulator required for motor circuit wiring.**

## Introduction

Neuronal circuit wiring requires developing axons to accurately sense and respond to environmental guidance cues to reach their correct synaptic targets. This axon navigation process therefore relies on the ability of the growth cone (GC) to integrate and translate external guidance signals into intracellular remodeling of its morphology in order to promote steering in the proper direction. Two closely related cellular processes have been shown to be critical for GC navigational behavior: cytoskeletal (Dent et al., 2011; Cammarata et al., 2016) and membrane (Itofusa and Kamiguchi, 2011; Steketee and Goldberg, 2012) dynamics. Several studies have indeed reported an asymmetric transport of vesicles to the GC periphery, followed by their exocytosis in response to attractive guidance signals (Tojima et al., 2007, 2011; Akiyama et al., 2016). Conversely, polarized endocytosis has been observed in response to repulsive signals (Tojima et al., 2010). In addition to regulating the supply or retrieval of plasma membrane at the axon tip, such membrane dynamics are crucial to regulate the amount of available guidance receptors at the GC surface (O'Donnell et al., 2009; Hines et al., 2010). Notably, signaling endosomes and their retrograde axonal transport to the soma in response to environmental cues have also been proposed to trigger signaling cascades that ultimately regulate exocytosis and membrane receptor integration at the GC plasma membrane (Deppmann et al., 2008; Ascaño et al., 2009; Steketee and Goldberg, 2012).

Bidirectional vesicular axonal transport therefore appears crucial for accurate axon navigation to occur. Importantly, this membrane trafficking takes place along the microtubule (MT) network (Tojima et al., 2007), suggesting a role for MT-based molecular motors in axon targeting processes. MT-based molecular motors and axonal transport have been largely studied in mature neurons for their role in neuronal homeostasis and survival (Hirokawa et al., 2010; Millecamps and Julien, 2013; Maday et al., 2014). While cytoplasmic dynein is known to mediate retrograde axonal transport, kinesins are mostly responsible for anterograde axonal transport (Maday et al., 2014). In the case of bidirectional transport, these opposite molecular motors are found together on the same cargo, where they act in a cooperative or competitive manner (Hancock, 2014). Although it is generally assumed that molecular motors should be required

[1]Sorbonne Université, University Pierre and Marie Curie-Université Paris 6, Institut de Biologie Paris Seine, Unité de Neuroscience Paris Seine, Centre National de la Recherche Scientifique, Unité Mixte Recherche 8246, Institut National de la Santé et de la Recherche Médicale U1130, Paris, France; [2]Department of Genetics and Developmental Biology, Institut Curie, Paris, France.

Correspondence to Coralie Fassier: coralie.fassier@upmc.fr; Jamilé Hazan: jamile.hazan@upmc.fr; M. Atkins' present address is Sorbonne Université, University Pierre and Marie Curie-Université Paris 6, Institut National de la Santé et de la Recherche Médicale U1270, Institut du Fer à Moulin, Paris, France; V. Bercier's present address is VIB-KU Leuven, Center for Brain and Disease Research, Leuven, Belgium; C. Fassier's present address is Sorbonne Université, Institut National de la Santé et de la Recherche Médicale Unité Mixte Recherche_U968, Centre National de la Recherche Scientifique Unité Mixte Recherche_7210, Institut de la Vision, Paris, France.

at earlier stages for axon navigation before synaptogenesis (Phillis et al., 1996; Tischfield et al., 2010), the precise mode of action and regulatory complexes through which they could control the accurate bidirectional cargo delivery required for GC steering remain poorly characterized. Notably, a few studies argue in favor of a role for molecular motors in MT asymmetrical invasion of the GC and coupling to the actin network during turning events (Myers et al., 2006; Grabham et al., 2007; Nadar et al., 2008, 2012; Kahn and Baas, 2016). However, their roles in other forms of transport, such as polarized vesicular axonal transport, have so far been mostly reported in the establishment and maintenance of neuronal polarity (Kapitein and Hoogenraad, 2011) or in axon elongation, but rarely in axon navigation per se (Schlager et al., 2010, 2014; van Spronsen et al., 2013; Deng et al., 2014; Lorenzo et al., 2014; Drerup et al., 2016).

Our team has recently identified the ATPase Fidgetin-like 1 (Fignl1) as a key player in zebrafish motor circuit wiring, via its regulation of MT plus-end dynamics (Fassier et al., 2018). Here, we report on a new role for Fignl1 in zebrafish axon navigation, via its regulation of bidirectional axonal vesicular trafficking. We show that Fignl1 forms a molecular complex with the Kif1bβ molecular motor and the dynein/dynactin motor adaptor Bicd1 (Matanis et al., 2002) and exhibits bidirectional mobility in navigating axons. Using loss- and gain-of-function approaches and in vivo live imaging, we provide compelling evidence supporting a key role for this complex in the restriction of dynein velocity in navigating axons and their subsequent targeting. Notably, we show that pharmacological inhibition of dynein rescues the axon pathfinding defects of Fignl1-depleted larvae. Overall, our work supports a model in which Fignl1 limits dynein velocity via its coupling to the opposite polarity-directed motor Kif1bβ and demonstrates the key role for such a mechanism in motor circuit wiring.

## Results

### Fignl1 directly binds the molecular motor Kif1bβ

We have previously unraveled critical roles for Fignl1 isoforms in the regulation of MT plus-end dynamics during zebrafish motor circuit wiring (Fassier et al., 2018). To further dissect the MT-based functions of this multifaceted ATPase in axon navigation, we have conducted a yeast two-hybrid screen. While sequence homologies between AAA$^+$ proteins are usually restricted to their C-terminal AAA domain, N-terminal regions are highly divergent and contain various domains that mediate the interactions with diverse substrates or adaptor proteins, thereby contributing to the functional diversity of such proteins (Patel and Latterich, 1998). We have thus used the N-terminal part of mouse fignl1 (aa 1–441) as bait to screen an E16 mouse embryonic brain cDNA library. Three independent clones containing cDNA fragments encoding the kif1bβ isoform of the kinesin-3 family kif1b molecular motors came out of this screen. The binding domain of kif1bβ for fignl1 encompasses a region of its specific "stalk" domain (aa 1180–1462), previously involved in cargo binding through different adaptor proteins (Fig. 1 A; Niwa et al., 2008; Xu et al., 2018). Coimmunoprecipitation (co-IP) assays from total protein extracts of COS-7 cells transfected with HA-tagged mouse fignl1 (HA-Ms_fignl1) and YFP-tagged human KIF1Bβ (YFP-Hu_KIF1Bβ) confirmed the physical interaction between these exogenously expressed proteins (Fig. 1, B and C). We further showed that this interaction is evolutionarily conserved since zebrafish Fignl1 (Dr_Fignl1-HA) has retained the ability to associate with YFP-Hu_KIF1Bβ (Fig. 1 D). Moreover, we showed that KIF1Bβ binds both full-length and N-terminally truncated Dr_Fignl1 isoforms (Fig. 1 E). However, studies in COS-7 cells revealed a stronger cytoplasmic colocalization between KIF1Bβ and N-terminally truncated Fignl1 isoforms compared with the full-length protein (Fig. 1 F). Notably, both proteins were shown to colocalize along some MT tracks (arrows, Fig. 1 F).

### Fignl1 colocalizes with Kif1bβ in zebrafish axons and shows bidirectional mobility

Fignl1 is highly enriched in developing primary (pMN at 24 hours post-fertilization [hpf]) and secondary (sMN at 48 hpf) motor neuron axons (Fassier et al., 2018). To investigate the role of Kif1bβ in Fignl1-driven motor axon navigation, we first assessed its expression pattern with regards to Fignl1. Using in situ hybridization, we showed that *Kif1bβ* transcript was strongly expressed at 24 and 48 hpf in the developing nervous system, including the ventral spinal cord where spinal motor neurons (SMNs) lie (Fig. 2 A). This spinal cord expression overlaps that of zebrafish Fignl1 by in situ hybridization and immunostaining (Fig. 2 B; Fassier et al., 2018). However, immunohistochemistry of zebrafish Kif1bβ could not be achieved due to the lack of selective antibodies. We thus turned to the *UAS*/GAL4 system to drive the expression of fluorescently tagged KIF1Bβ and Fignl1 in developing zebrafish neurons using transient transgenesis. Co-expression of 14*UAS*:YFP-Hu_KIF1Bβ and 14*UAS*:Fignl1-TagRFP (Fignl1-TRFP) constructs in neurons could only be driven by the Tg(*HuC*:GAL4) line. Furthermore, in this line, co-expression of both constructs was rare and faint in SMNs. These technical limitations led us to assess their colocalization in other spinal neurons using spinning-disk confocal microscopy (Fig. 2, C and D). YFP-Hu_KIF1Bβ and Fignl1-TRFP showed a vesicular pattern along spinal neuron axons (Fig. 2, C and D)—which was consistent with their respective distribution in mouse (Charalambous et al., 2013) and zebrafish motor (Fig. 2 E–G) neurons—and co-localized onto some vesicles (arrows, Fig. 2, C and D). This result incited us to analyze Fignl1-TRFP mobility in navigating SMN axons of Tg(*HuC*:GAL4; 14*UAS*:Fignl1-TRFP) transgenic larvae using live spinning-disk confocal microscopy. Kymogram analysis of Fignl1-TRFP mobility revealed that this ATPase is transported in both the anterograde and retrograde directions within SMN axons at mean velocities that are coherent with fast molecular motor-based axonal transport (0.28 µm/s$^{-1}$ and 0.31 µm/s$^{-1}$, respectively; Fig. 2, E–G; and Video 1). These data may point out a role for motor-based axonal transport in Fignl1-dependent SMN axon targeting.

### Kif1bβ loss of function affects zebrafish motor axon pathfinding and locomotor behavior in a similar way to Fignl1 depletion

To test this hypothesis, we next analyzed SMN development in control and *kif1b*$^{st43}$ mutants, which harbor a mutation in the

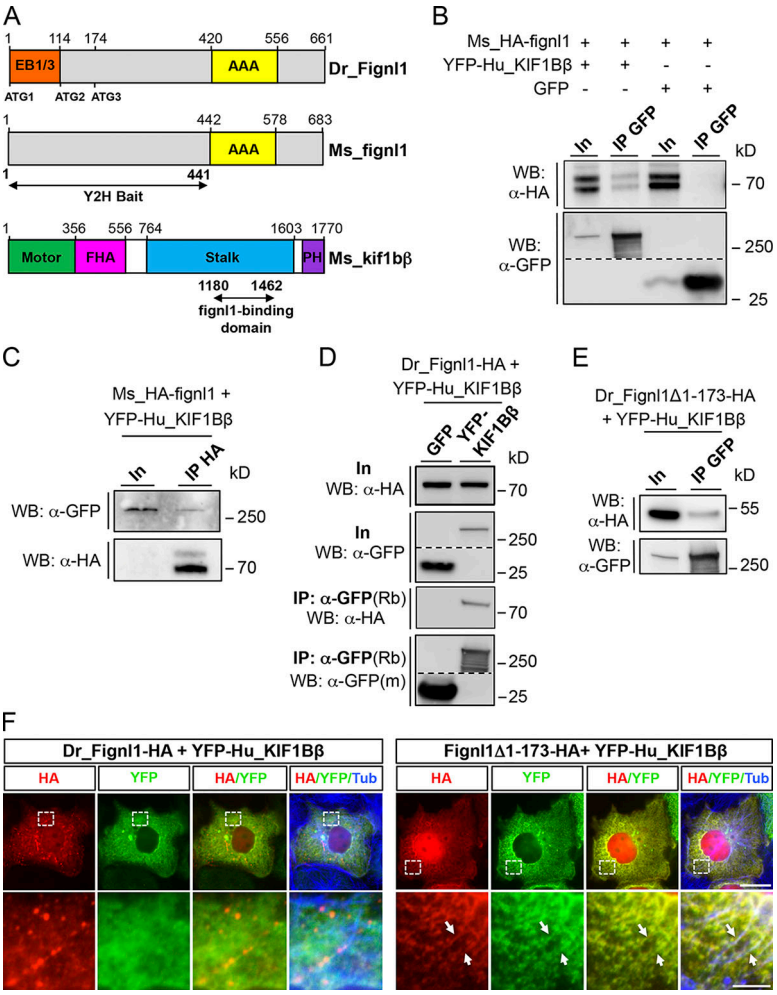


Figure 1. **Identification of the kif1bβ molecular motor as a direct binding partner of Fignl1. (A)** Schematic representation of zebrafish Fignl1 (Dr_Fignl1), mouse fignl1 (Ms_fignl1), and mouse kif1bβ (Ms_ kif1bβ). Specific domains are shown as boxes, and numbers indicate amino acids that delineate domain frontiers. EB1/3, EB-binding domain; AAA, ATPase domain; Motor, MT-binding domain; FHA, forkhead-associated domain; PH, Pleckstrin homology; Y2H, yeast two-hybrid screen. ATG1, ATG2, and ATG3 indicate alternative translation start sites identified in the zebrafish *fignl1* sequence. Black arrows summarize the results of the yeast two-hybrid assay. **(B and C)** Ms_HA-fignl1 specifically associates with YFP-Hu_KIF1Bβ. Co-IP of Ms_HA-fignl1 and YFP-Hu_KIF1Bβ from protein extracts of COS-7 cells transfected with YFP-Hu_KIF1Bβ (B and C) or GFP (B) and Ms_HA-fignl1. **(D and E)** Co-IPs of Dr_Fignl1-HA (D) and Dr_Fignl1Δ1-173-HA (E) with YFP-Hu_KIF1Bβ. Co-IPs were performed from protein extracts of COS-7 cells transfected with YFP-Hu_KIF1Bβ and Dr_Fignl1-HA (D) or Dr_Fignl1Δ1-173-HA (E). **(B–E)** Immunoprecipitations were performed with GFP- (B, D, and E) or HA-trap antibodies (C). Immunoprecipitated and coimmunoprecipitated proteins were revealed by Western blot using HA or GFP antibodies. In, Input; IP, immunoprecipitation; WB, Western blot; Rb, rabbit; m, mouse. **(F)** COS-7 cells transfected with YFP-Hu_KIF1Bβ and Dr_Fignl1-HA or Dr_Fignl1Δ1-173-HA and immunolabeled with HA, GFP, and tyrosinated tubulin (Tub) antibodies. Bottom panels are higher magnifications of the boxed regions in the corresponding upper panels. White arrows in the right-hand panels indicate colocalization events that occur along MTs. Scale bars, 20 µm for upper panels and 5 µm for lower panels.

*Kif1b* motor domain (Lyons et al., 2009). *Kif1b* mutation did not affect pMN axon outgrowth, unlike *Fignl1* knockdown (Fig. S1 A; Fassier et al., 2018). However, *kif1b*$^{st43}$ mutants showed sMN axon pathfinding defects, which were restricted to rostrally projecting-like sMN (RoP-like sMN; Fig. 3, A–D) and overlapped the RoP-like sMN defects observed in mildly affected *Fignl1* morphants (i.e., embryos injected with *Fignl1* morpholino; Fassier et al., 2018) and *fignl1*$^{sa22254}$ mutants—harboring a mutation that results in the truncation of the ATPase domain (Fig. 3 E). Indeed, some rostral nerves of *kif1b*$^{st43}$ mutants failed to develop properly in a normal muscle environment (Fig. S1 B) and appeared defasciculated, split (arrows and arrowheads, respectively, Fig. 3 A), or to a lesser extent absent, compared with rostral nerves of control siblings (empty arrowheads, Fig. 3, A and C). The mean number of defasciculated/split or missing rostral nerves per larva was significantly increased in *kif1b*$^{st43}$ mutants compared with controls (Fig. 3, B and C). In contrast, the number of rostral nerves that abnormally turned caudally was unchanged (Fig. 3 D). Notably, a significant increase in the number of defasciculated or split rostral nerves was also observed between *fignl1*$^{sa22254/+}$ heterozygous mutant and control larvae (Fig. 3, E and F), while homozygous *fignl1*$^{sa2225/sa22254}$ mutants displayed a stronger phenotype characterized by an increased number of missing rostral nerves compared with *fignl1*$^{+/+}$ control larvae (Fig. 3, E and G). Altogether, these results revealed a dose-effect impact of Fignl1 on RoP-like sMN development (Fig. 3, F–H) and strengthened our morpholino data (Fassier et al., 2018).

Since the *kif1b*$^{st43}$ mutation alters the *Kif1b* motor domain—common to both Kif1bα and Kif1bβ splice isoforms—we then used morpholinos targeted against a splice site junction specific to each isoform (morpholino oligonucleotide [MO] *Kif1bα* and MO *Kif1bβ*; Lyons et al., 2009) to silence their expression and assess their respective roles in RoP-like sMN axon pathfinding (Fig. 3, I–M; and Fig. S2 for the knockdown strategy). Notably, MO *Kif1bβ*-injected larvae exhibited defasciculated/split rostral nerves as *kif1b*$^{st43}$ mutants and *Fignl1*-depleted larvae (Fig. 3, I–L). By contrast, no obvious pathfinding defects of RoP-like axons were observed in MO *Kif1bα*-injected larvae (Fig. 3, I and M), despite similar knockdown efficiencies of the *Kif1bα* and *Kif1bβ* morpholinos—when injected at 0.7 and 1.4 pmol, respectively (Fig. S2). Moreover, injection of the *Kif1bβ* morpholino in *kif1b*$^{st43}$ mutants did not exacerbate the sMN phenotype compared with non-injected mutant larvae (Fig. 3, N and O), further confirming the specificity of the axon pathfinding phenotypes associated with *Kif1bβ* knockdown and the validity of the *Kif1bβ* morpholino. Finally, the sMN defects of *Kif1bβ* morphant larvae were associated with locomotor deficits in the touch-evoked escape response test, which were reminiscent of those described in *Fignl1*

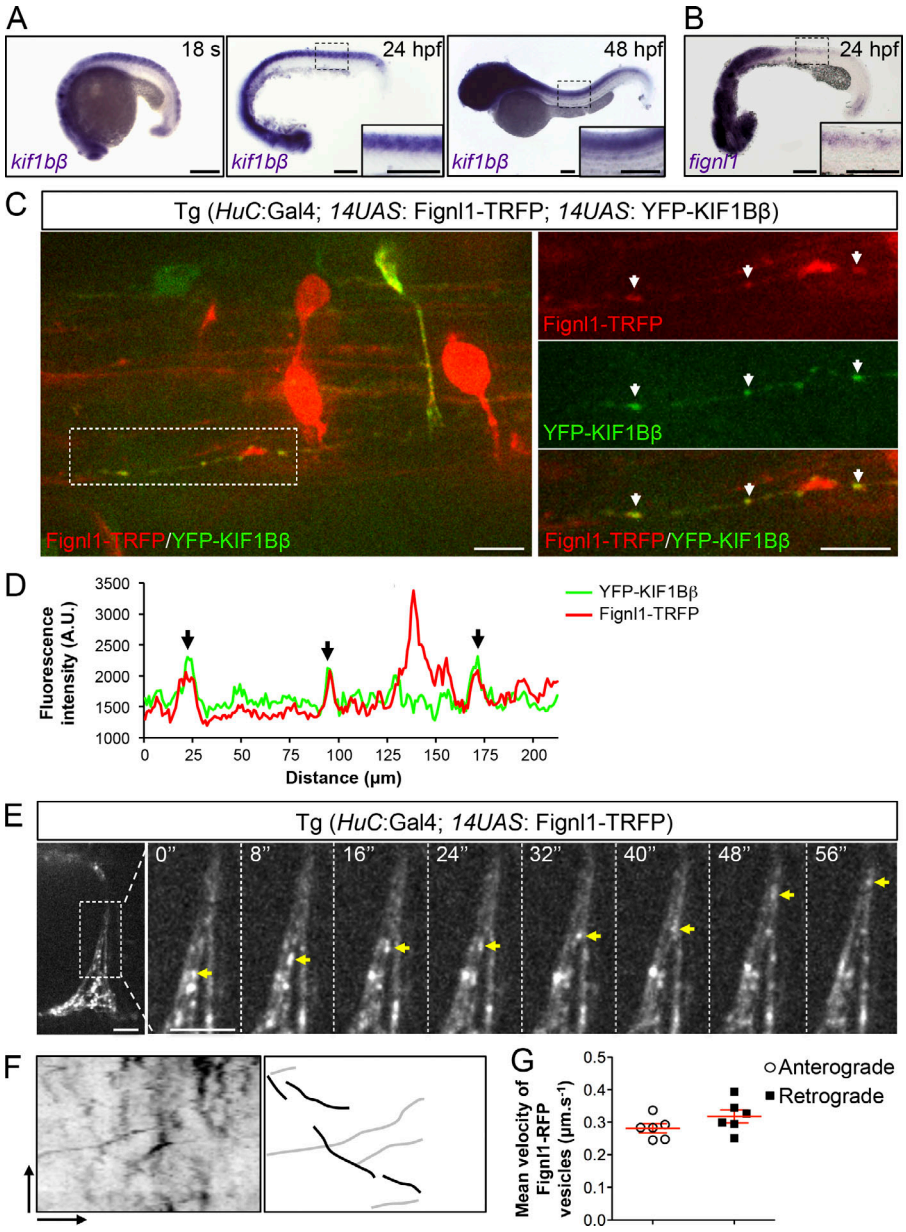


Figure 2. **Fignl1 colocalizes with the kinesin motor KIF1Bβ and is actively transported in zebrafish sMN axons. (A)** Whole-mount in situ hybridization with *kif1bβ* antisense riboprobe at the 18-somite stage (18 s), 24 and 48 hpf. **(B)** Whole-mount in situ hybridization of 24-hpf embryos with *fignl1* antisense probe. **(A and B)** Images are lateral views of the embryo, anterior to the left. Insets are higher magnifications of the spinal cord. Scale bars, 200 µm. **(C)** Z-stack of spinning-disk confocal images showing Fignl1 and KIF1Bβ colocalization in zebrafish axons of 56-hpf Tg(*HuC*:GAL4; 14*UAS*: Fignl1-TRFP; 14*UAS*: YFP-Hu_KIF1Bβ) transgenic larvae. Right-hand panels are higher magnifications of the boxed region of the corresponding left-hand panel. Scale bars, 10 µm. **(D)** Fluorescence intensity profile of Fignl1-TRFP and YFP-Hu_KIF1Bβ along the axon boxed in C. **(C and D)** White and black arrows indicate Fignl1 and KIF1Bβ colocalization. **(E)** Still images from time-lapse recordings of Fignl1-TRFP axonal transport in sMN axons of 56-hpf Tg(*HuC*:GAL4; 14*UAS*: Fignl1-TRFP) transgenic larvae. Right-hand panels are higher magnifications of the axon boxed in the left-hand panel. Yellow arrowheads track a Fignl1-TRFP-positive vesicle moving in the retrograde direction. Scale bars, 7.4 µm. **(F)** Left: Representative kymogram of Fignl1-TRFP motility in sMN axons. Right: schematic kymogram illustrating anterograde (black) and retrograde (gray) Fignl1-TRFP traces. Vertical scale bar, 85 s; horizontal scale bar, 5.6 µm. **(G)** Mean anterograde and retrograde velocities of Fignl1-TRFP-positive vesicles in sMN axons ($n$ = 6) selected randomly from four transgenic fish. Mean velocities per axon were extracted from 50 kymogram traces. A.U., arbitrary units.

morphant larvae and characterized by reduced swimming speed (60% for *Kif1bβ* morphant versus controls, Fig. S3, A and B; 69% for *Fignl1* morphants versus controls, Fassier et al., 2018) and covered distances (30% reduction for *Kif1bβ* morphant versus controls, arrowheads, Fig. S3, A and C; 70% for *Fignl1* morphants versus control, Fassier et al., 2018) compared with *Kif1bα* morphant or control larvae. This reduced motility was not associated with obvious developmental defects of additional key players in the zebrafish startle response, such as the Mauthner cells or muscle fibers (Fig. S3, D and E). Altogether, our data unveil a critical role for Kif1bβ in the establishment of RoP-like sMN axon connectivity and suggest a cooperative role for this molecular motor and Fignl1 in this developmental process.

### Kif1bβ is not required for Fignl1 enrichment in GCs

Kif1b was recently shown to promote peripheral sensory axon outgrowth by localizing the MT regulator SCG10 in GCs (Drerup et al., 2016). To test whether Fignl1 axonal distribution also relies on Kif1bβ, we performed whole-mount immunolabeling of Fignl1 in control and *kif1b*$^{st43}$ mutant embryos, which failed to show striking changes in Fignl1 subcellular distribution (Fig. 4, A–D). Indeed, the analysis of the Fignl1 fluorescence intensity profile along SMN axons revealed that Fignl1 was properly enriched at the distal tip of *kif1b*$^{st43}$ mutant axons (Fig. 4 B). Consistently, the mean fluorescence intensity of Fignl1 within SMN GCs (i.e., related to the GC area; Fig. 4 C) was indistinguishable between control and *kif1b*$^{st43}$ mutant embryos. Fignl1 distribution also appeared unchanged in *kif1b*$^{st43}$ mutant ventral longitudinal fasciculus axons, another population of axons characterized by a clear enrichment of Fignl1 in the GC (Fig. 4 D; Fassier et al., 2018). These data suggest that Fignl1 may not be a Kif1bβ cargo, unlike SCG10 (Drerup et al., 2016).

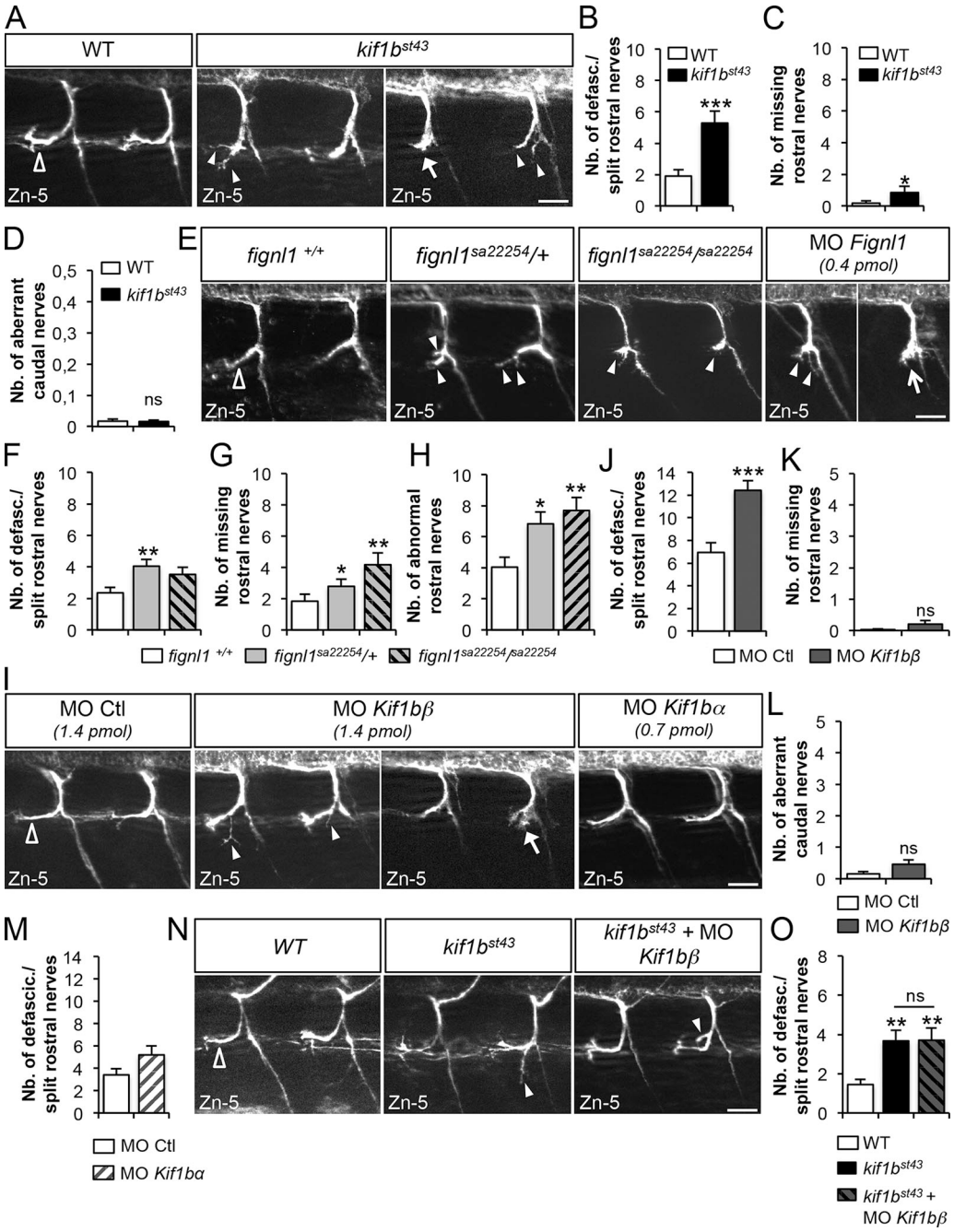


Figure 3. **Loss of Kif1bβ isoform leads to RoP-like sMN axon pathfinding defects that are reminiscent of those observed in *Fignl1* morphants and mutants. (A)** Immunolabeling of sMN in 56-hpf control and *kif1b*$^{st43}$ homozygous mutants using the Zn-5 antibody. **(B–D)** Mean number of defasciculated/split (B), missing (C), or mistargeted (i.e., caudally projecting; D) rostral nerves per embryo. Quantifications were performed in 23 control and 26 *kif1b*$^{st43}$ mutant larvae pooled from three independent experiments. **(E)** Immunolabeling of sMN in 56-hpf control (*fignl1*$^{+/+}$), *fignl1* heterozygous (*fignl1*$^{sa22254/+}$), or homozygous (*fignl1*$^{sa22254/sa22254}$) mutant and *Fignl1* morphant (Fassier et al., 2018) larvae using the Zn-5 antibody. **(F–H)** Mean number of defasciculated/split (F), missing (G), or abnormal (H) rostral nerves per embryo. Quantifications were performed in 28 *fignl1*$^{+/+}$, 27 *fignl1*$^{sa22254/+}$, and 20 *fignl1*$^{sa22254/sa22254}$ larvae pooled from three independent experiments. **(I)** Immunostaining of sMN in 56-hpf larvae injected with control, *Kif1bβ*, and *Kif1bα* morpholinos using the Zn-5 antibody. **(J–M)** Mean number of defasciculated/split (J and M), missing (K), or mistargeted (i.e., caudally projecting; L) rostral nerves per embryo. Quantifications were performed in 42 control and 37 *Kif1bβ* morphant larvae (J–L), and 18 control and 16 *Kif1bα* morphant larvae (M), pooled from three independent experiments. **(N)** Immunolabeling of sMN in 56-hpf control and *kif1b*$^{st43}$ homozygous mutants injected or not with the *Kif1bβ* morpholino. **(O)** Mean number of defasciculated/split rostral nerves per embryo. **(A, E, I, and N)** Images are lateral views of the trunk, anterior to the left. Empty arrowheads show control rostral nerves. Arrowheads and arrows indicate rostral nerves that are respectively abnormally split or defasciculated. Scale bars, 20 µm. **(B–D, F–H, J–M, and O)** Quantifications were performed in 12 (F–H) or 24 (B–D, J–M, and O) spinal hemisegments per embryo. *, P ≤ 0.05; **, P ≤ 0.01; ***, P ≤ 0.001; ns, non-significant; unpaired two-tailed *t* test (B, D, J, and M), Mann–Whitney *t* test (C and K–L), Kruskal–Wallis ANOVA test with Dunn's post-test (F, G, and O), or one-way ANOVA test with Bonferroni's multiple comparison post test (H). Error bars are SEM. Nb, number; defasc., defasciculated; Ctl, control.

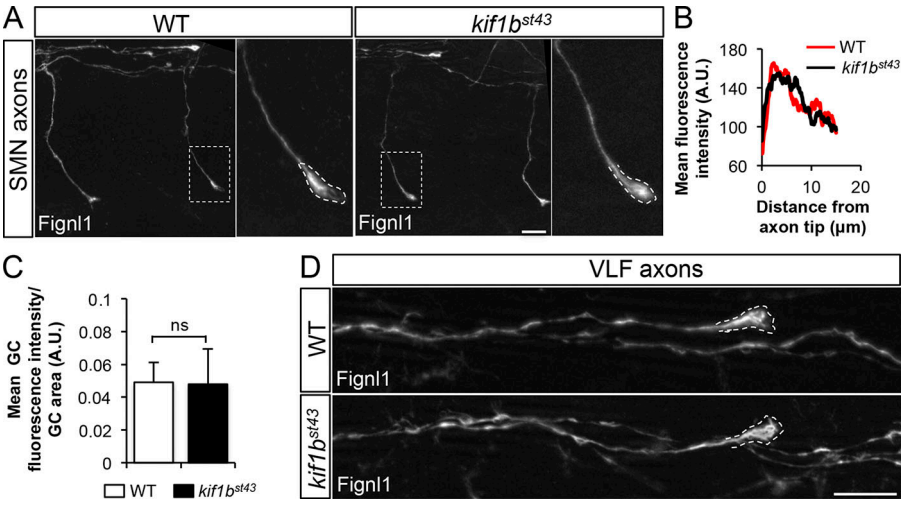


Figure 4. **Kif1b loss of function does not affect Fignl1 enrichment in GCs. (A)** In toto immunohistochemistry of Fignl1 in 26-hpf control and *kif1b*$^{st43}$ mutant embryos focusing on SMN axons. The right-hand side of each genotype panel represents a higher magnification of the distal axon boxed in the corresponding left-hand panel. **(B)** Mean fluorescence intensity profile of Fignl1 along the distal portion of control ($n$ = 35) and *kif1b*$^{st43}$ ($n$ = 78) mutant SMN axons. **(C)** Mean fluorescence intensity of Fignl1 staining in control ($n$ = 41) and *kif1b*$^{st43}$ ($n$ = 50) spinal motor GCs with respect to the GC area. ns, nonsignificant ($P > 0.05$); unpaired two-tailed $t$ test. Quantifications were performed in control ($n$ = 9) and *kif1b*$^{st43}$ ($n$ = 13) embryos pooled from two independent experiments. Error bars are SEM. A.U., arbitrary units. **(D)** In toto immunohistochemistry of Fignl1 in 26-hpf control and *kif1b*$^{st43}$ mutant embryos focusing on axons from the ventral longitudinal fasciculus. **(A and D)** Images are lateral views of the trunk, anterior to the left. Dashed lines delineate the GC surface. Scale bars, 10 µm.

### Kif1bβ and Fignl1 regulate bidirectional axonal transport of Rab3 vesicles by restricting dynein-based transport velocity in navigating axons

To further dissect the relationship between Kif1bβ and Fignl1 in axon navigation, we next investigated the influence of Fignl1 on Kif1bβ-mediated axonal transport. Kif1bβ was shown to be critical for Rab3-positive synaptic vesicle transport in mammalian hippocampal neurons (Niwa et al., 2008). Accordingly, we first assessed whether Rab3 vesicles were transported by Kif1bβ in zebrafish SMN axons and could thus be used as a readout of Kif1bβ-mediated transport activity. To analyze Rab3 vesicular trafficking in vivo in isolated navigating SMN axons, Tg(mnGFF7) embryos expressing GAL4 in SMN (Asakawa et al., 2008, 2013) were sequentially injected with a *UAS*:Rab3-Dendra2 plasmid and either the *Kif1bβ* or a control morpholino (Fig. 5 A). Since we had previously validated the specificity of the *Kif1bβ* morpholino with *kif1b*$^{st43}$ mutants (Fig. 3), we here chose to use *Kif1bβ* morphant larvae—rather than *kif1b*$^{st43}$ mutants—to rule out a potential contribution of the Kif1bα isoform in Rab3 vesicular axonal transport. Kymogram analysis of Rab3-Dendra2 time-lapse recordings from 50-hpf control and *Kif1bβ* morphant Tg(mnGFF7) larvae showed that Kif1bβ depletion increased Rab3 axonal transport velocities in both anterograde and retrograde directions in SMN axons (Fig. 5, B–D), a phenotype previously associated with other kinesin knockdown in non-neuronal cells (Schlager et al., 2014). Conversely, mean run lengths (i.e., distance traveled between two pauses) were unchanged in both directions following *kif1bβ* knockdown (Fig. 5, B, E, and F). These data showed a role for Kif1bβ in Rab3 vesicular trafficking during zebrafish SMN axon navigation. In light of these results, we next investigated the impact of *Fignl1* knockdown on Rab3 axonal transport (Fig. 5, A, B, G–J, and L). Interestingly, the retrograde velocities of Rab3-Dendra2 vesicles were significantly increased in Fignl1-depleted SMN axons compared with control axons, while the anterograde speeds remained unchanged (Fig. 5, G and H). Nevertheless, Fignl1 depletion was also associated with a significant decrease in Rab3-Dendra2 vesicular run lengths in the anterograde but not in the retrograde direction (Fig. 5, I and J), suggesting a dual role for Fignl1 in Kif1bβ processivity and dynein speed restriction. Finally, the mean number of static vesicles remained unchanged in Kif1bβ- or Fignl1-depleted SMN axons compared with control axons (Fig. 5, K and L). Our results therefore suggest that both proteins might regulate Rab3 bidirectional axonal transport, most likely via the restriction of dynein-based transport velocity.

### Fignl1 forms a molecular complex with Kif1bβ, the dynein/dynactin adaptor protein Bicd1, and the dynactin subunit dynactin 1

Supporting this hypothesis, the motor adaptor protein Bicd1, reported to recruit the dynein/dynactin complex to cargoes (Matanis et al., 2002; Hoogenraad and Akhmanova, 2016), was identified as a partner of Fignl1 in our yeast two-hybrid screen (Fig. 6 A). Indeed, two independent clones containing *bicd1* cDNA fragments were pinpointed for their direct interaction with the fignl1 N-terminal part (aa 1–441). This screen allowed us to map the fignl1-binding domain between aa 684 and 813 of the bicd1 sequence, which overlaps with its CC3 coil-coiled domain (Fig. 6 A), previously involved in the binding of Rab6 vesicles (Matanis et al., 2002). GFP-Ms_bicd1 and Dr_Fignl1-HA showed a strong colocalization onto cytoplasmic vesicles of transfected COS-7 cells (arrowheads, Fig. 6 B). Furthermore, co-IP assays from total protein extracts of COS-7 cells transfected with HA-Ms_fignl1 or Dr_Fignl1-HA and GFP-Ms_bicd1 confirmed the physical interaction between these exogenously expressed proteins and demonstrated that both full-length and N-terminally truncated Fignl1 isoforms associate with GFP-Ms_bicd1 (Fig. 6 C). To assess whether Fignl1 and bicd1 could form a molecular complex together with KIF1Bβ, we first tested the interaction between Flag-Ms_bicd1 and YFP-Hu_KIF1Bβ following their expression in

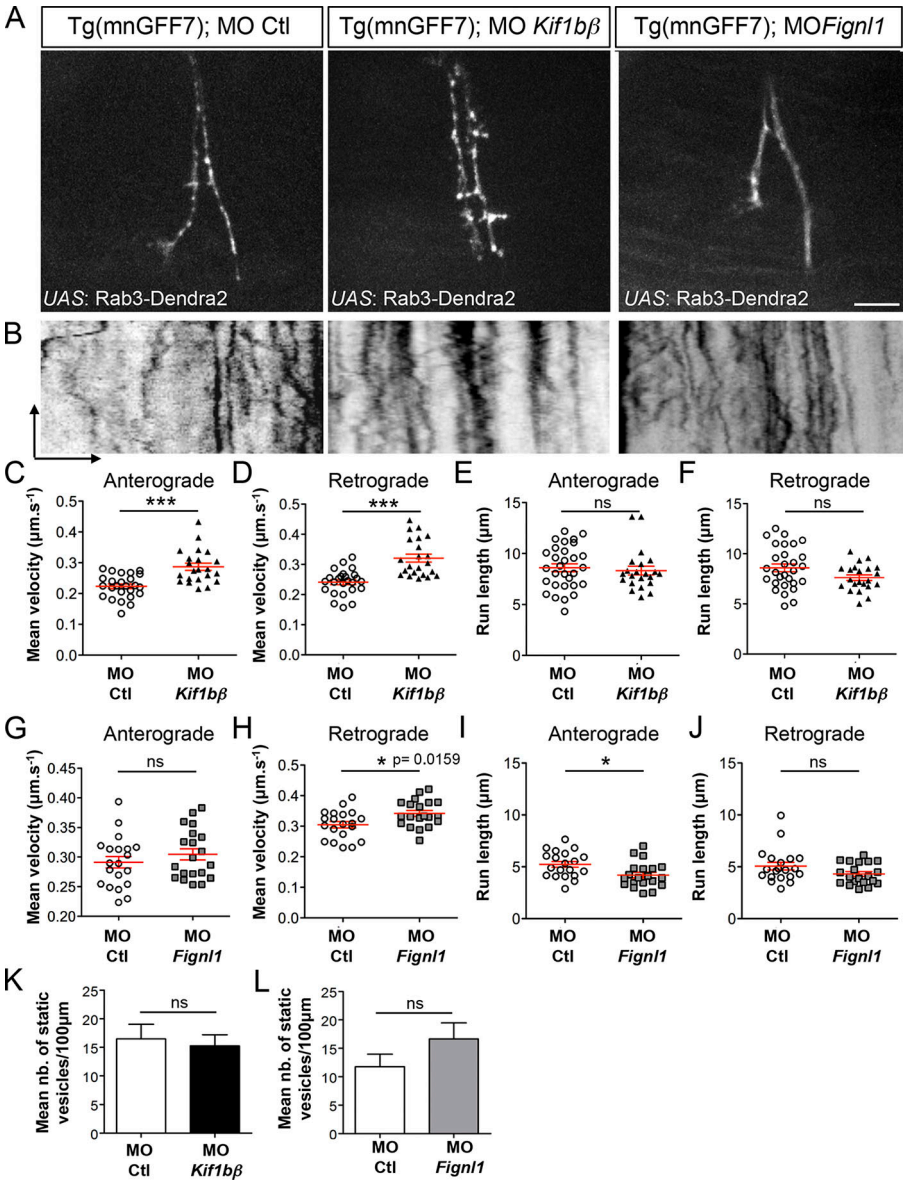


Figure 5. **The loss of Kif1bβ or Fignl1 similarly increases dynein-based Rab3 retrograde transport velocity. (A)** Still images extracted from time-lapse recordings of Rab3-Dendra2 vesicles in SMN axons of 50-hpf Tg(mnGFF7) larvae injected with control MO (MO Ctl), MO *Kif1bβ*, or MO *Fignl1* and a *UAS*:Rab3-Dendra2 plasmid. Scale bar, 10 µm. **(B)** Representative kymograms of Rab3-Dendra2 vesicle transport in control, *Kif1bβ* and *Fignl1* morphant sMN axons. Vertical black lines represent static vesicles. Vertical scale bar, 2 min; horizontal scale bar, 10 µm. **(C–J)** Mean anterograde (C, E, G, and I) and retrograde (D, F, H, and J) velocities (C, D, G, and H) or run lengths (E, F, I, and J) of Rab3-vesicles measured in control ($n$ = 20; C–J), *Kif1bβ* ($n$ = 20; C–F), or *Fignl1* morphant ($n$ = 20; G–J) SMN axons. *, P ≤ 0.05, ***, P ≤ 0.001, ns, nonsignificant (P > 0.05); unpaired two-tailed $t$ test with Welch's correction and Mann–Whitney test for velocity and run length comparisons, respectively. Error bars are SEM. **(K–L)** Mean number of static vesicles related to a 100-µm axon portion. ns, nonsignificant (P > 0.05); Mann–Whitney test. Error bars are SEM.

COS-7 cells. As expected, Flag-Ms_bicd1 was efficiently copelleted with YFP-Hu_KIF1Bβ, but not with the control GFP (Fig. 6 D). Moreover, Dr_Fignl1-HA and endogenous or exogenous (YFP-Hu_KIF1Bβ) KIF1B were found to copellet with the dynein adaptors bicd1 (Flag-Ms_bicd1; Fig. 6 E) and dynactin 1 (Fig. 6 F) in COS-7 cells, establishing the presence of a common molecular complex including these four members. The existence of such a complex further supports a role for Fignl1 in the regulation of bidirectional axonal transport.

### Disrupting the link between Fignl1 and Bicd1 affects RoP-like sMN axon pathfinding as Fignl1 or Kif1bβ loss of function does

To investigate the physiological relevance of the Bicd1/Fignl1/Kif1bβ complex in motor axon pathfinding, we next analyzed *bicd1* expression in the zebrafish developing nervous system. Due to an ancestral genome duplication in teleost fish, the mammalian *bicd1* gene has two orthologues in the zebrafish genome: *bicd1(K18)* located on chromosome 18, and *bicd1(K4)* mapped to chromosome 4. We thus performed whole-mount in situ hybridization on 24-hpf embryos with specific antisense riboprobes designed against each *bicd1* paralogue. *Bicd1(K18)* expression was detected in both sensory Rohon–Beard neurons (bracket, Fig. 7 A) and SMN in the developing spinal cord (arrowheads, Fig. 7 A). By contrast, *bicd1(K4)* expression was restricted to SMN (arrowheads, Fig. 7 A). These expression patterns of *bicd1* paralogues were thus consistent with a potential role of Fignl1 and Kif1bβ in SMN axon pathfinding. Since bicd proteins are critical adaptors for the dynein/dynactin complex motility (Schlager et al., 2014; Jha et al., 2017), we used a dominant-negative strategy—based on the overexpression of the bicd1-binding domain for Fignl1—to block the Fignl1/Bicd1 interaction in vivo in zebrafish neurons. The bicd1-binding domain for Fignl1 (i.e., CC3 domain, which differs from the dynein/dynactin-binding domain) identified via our yeast two-hybrid screen was first refined using a set of GFP-tagged bicd1_CC3 deletion constructs in co-IP assays with HA-Fignl1 (Fig. 7, B and

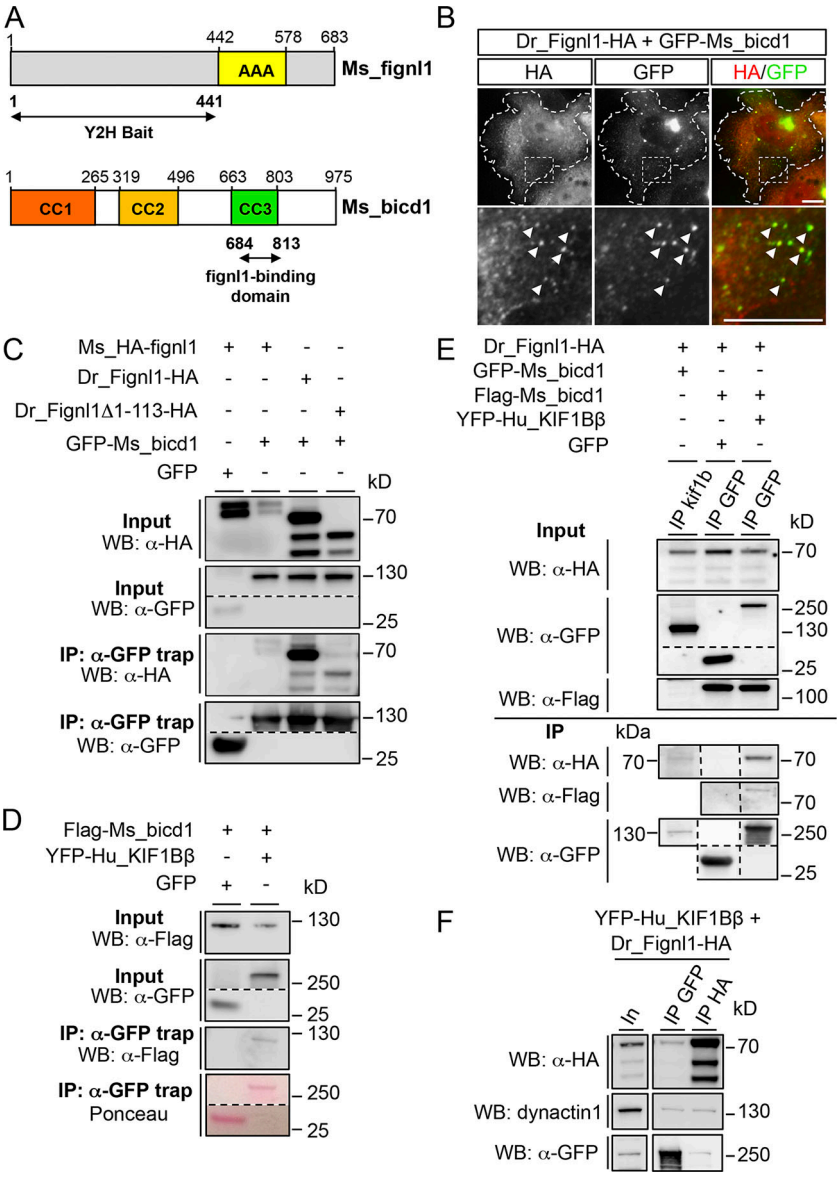


Figure 6. **Fignl1 directly binds the dynein/dynactin motor adaptor bicd1 in a protein complex including KIF1Bβ and dynactin 1. (A)** Schematic representation of Ms_fignl1, Ms_bicd1, and their respective binding domains identified through a yeast two-hybrid screen (Y2H; black arrows). Specific domains are shown as boxes. Numbers indicate amino acids that delineate domain frontiers. AAA, ATPase domain; CC1, CC2, and CC3, coil-coiled domains. **(B)** COS-7 cells transfected with GFP-Ms_bicd1 and Dr_Fignl1-HA, and immunolabeled with HA and GFP antibodies. Dashed line delimits the transfected cell. Bottom panels represent higher magnifications of boxed regions in corresponding upper panels. Arrowheads indicate colocalization between HA-Fignl1 and GFP-bicd1 onto cytoplasmic vesicles. Scale bars, 10 µm. **(C)** Fignl1 associates with bicd1. Co-IP of Fignl1 isoforms and bicd1 from protein extracts of COS-7 cells transfected with GFP-Ms_bicd1 or GFP, Ms_ HA-fignl1, Dr_Fignl1-HA, or Dr_Fignl1Δ1-113-HA. **(D)** KIF1Bβ associates with bicd1. Co-IP of KIF1Bβ and bicd1 from protein extracts of COS-7 cells transfected with YFP-Hu_KIF1Bβ and Flag-Ms_bicd1. **(E and F)** Fignl1 is part of a protein complex including KIF1Bβ and the dynein adaptors bicd1 (E) and dynactin 1 (F). **(E)** Left-hand well: Co-IP of exogenous Fignl1 and bicd1 with endogenous kif1b from protein extracts of COS-7 cells transfected with Dr_Fignl1-HA and GFP-Ms_bicd1. Middle and right-hand wells: Co-IP of exogenous Fignl1, bicd1, and KIF1Bβ from protein extracts of COS-7 cells transfected with Dr_Fignl1-HA, Flag-Ms_bicd1, and YFP-Hu_KIF1Bβ or GFP. Immunoprecipitations were performed with GFP-trap (C–F), KIF1B (E), or HA (F) antibodies. Immunoprecipitated and coimmunoprecipitated proteins were revealed by Western blot using anti-tag or KIF1B and dynactin 1 antibodies or by Ponceau staining. IP, immunoprecipitation; WB, Western blot.

C). The resulting restricted domain (GFP-bicd1$^{713\text{-}802}$) or the GFP alone was then cloned in a Tol2 *UAS* vector and injected in the Tg (*HuC*:GAL4) driver line. Transgenic embryos were immunolabeled at 56-hpf with GFP and sMN-specific (Zn-5) antibodies. The number of GFP-positive and -negative rostral nerves that appeared normal, desfasciculated/split, missing, or mistargeted was quantified in each transgenic embryo. Mosaic expression of GFP-bicd1$^{713\text{-}802}$ in neurons (Fig. 7 D) led to a specific and significant increase in the number of GFP-positive versus GFP-negative defasciculated/split rostral nerves, in contrast to the expression of the GFP alone (Fig. 7, E and F). Thus, impeding the Bicd1/Fignl1 interaction in zebrafish motor neurons led to RoP-like sMN axon pathfinding errors that mimic those associated with Fignl1 or Kif1bβ depletion. Altogether, these results demonstrate that the interaction between Fignl1 and the dynein adaptor Bicd1 is required for Fignl1/Kif1bβ-mediated sMN axon navigation, presumably to restrict dynein velocity, as suggested by our Rab3 live imaging experiments (Fig. 5).

### Fignl1 controls RoP-like sMN axon pathfinding by limiting dynein activity

To confirm the role of Fignl1 as a negative regulator of dynein-based transport in motor circuit wiring, we assessed whether altering dynein/dynactin activity, either through dynein pharmacological inhibition or by the depletion of dynactin 1, a key subunit of the dynein activator complex, would affect RoP-like sMN axon pathfinding as Fignl1 overexpression did (i.e., the presence of caudally mistargeted or missing rostral nerves; Fig. 8, A–F). WT zebrafish larvae were treated at 46 hpf with 4 µM of the dynein inhibitor Ciliobrevin D or the vehicle alone (DMSO) and subsequently fixed at 56-hpf to analyze sMN axon trajectories. While the vast majority of rostral nerves failed to form in WT larvae treated with 4 µM Ciliobrevin D (arrow, Fig. 8, A and B), some of the remaining ones aberrantly grew caudally along the horizontal myoseptum (full arrowhead, Fig. 8 A) compared with rostral nerves of DMSO-treated larvae (empty arrowhead, Fig. 8 A). These axon pathfinding defects were also

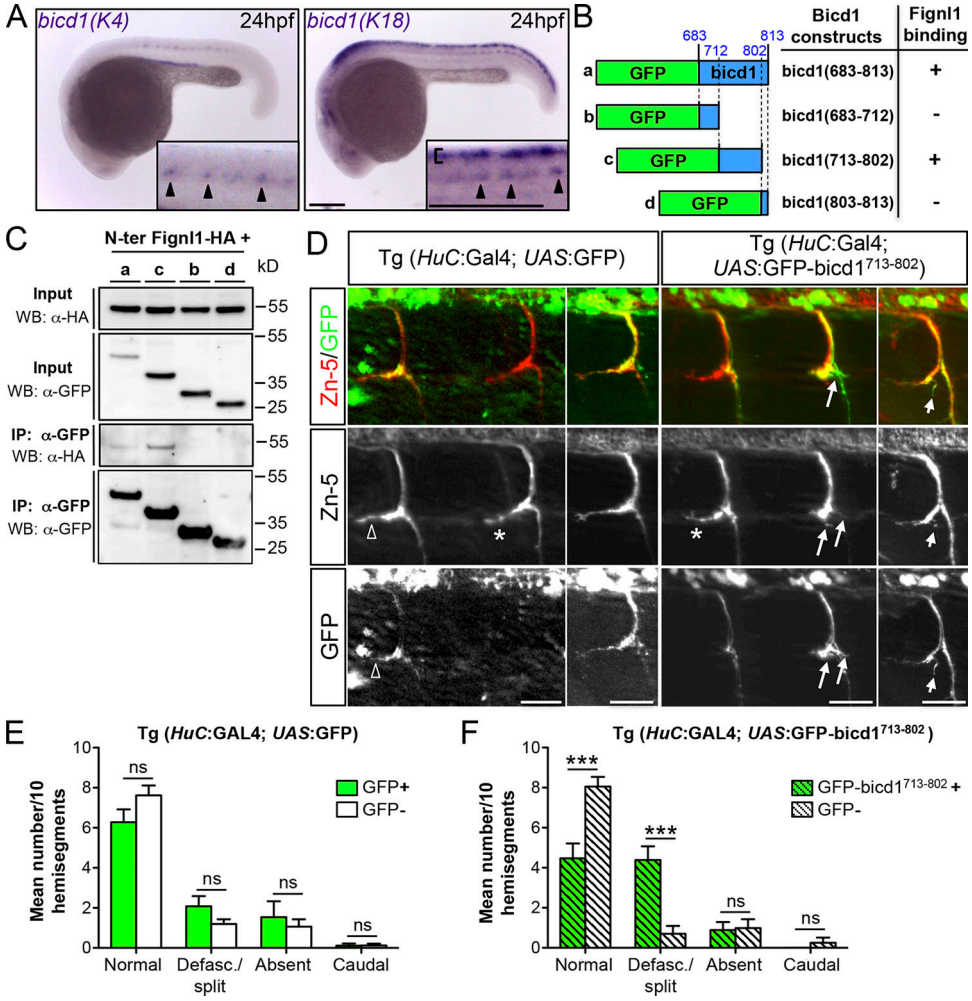


Figure 7. **Impeding the interaction between Bicd1 and Fignl1 in motor neurons affects RoP-like sMN axon pathfinding as Fignl1 and Kif1bβ loss of function does. (A)** Whole-mount in situ hybridization with *bicd1(K4)* and *bicd1(K18)* antisense probes on 24-hpf embryos. Images are lateral views of the embryo, anterior to the left. Insets are higher magnifications of the spinal cord. Arrowheads point at SMN expression of both zebrafish *bicd1* paralogues. Bracket indicates *bicd1(K18)* expression in Rohon–Beard sensory neurons. Scale bars, 200 µm. **(B)** Schematic representation of the bicd1 constructs used in co-IP assays with Fignl1-HA and their ability to bind Fignl1. **(C)** Western blots showing the co-IP results summarized in panel B. Co-IPs were performed from protein extracts of COS-7 cells transfected with Dr_Fignl1-HA and the different bicd1 constructs mentioned in panel B using a GFP-trap antibody. Immunoprecipitated and coimmunoprecipitated proteins were revealed by immunoblot using anti-HA and GFP antibodies. IP, immunoprecipitation; WB, Western blot. The bicd1(713–802) domain is required to bind Fignl1. **(D)** Neuronal-targeted overexpression of the bicd1(713–802) domain was used in a dominant-negative approach to block endogenous interaction between Bicd1 and Fign1 in neurons. Immunolabeling of 56-hpf Tg(*HuC*:GAL4; *UAS*:GFP) and Tg(*HuC*:GAL4; *UAS*:GFP-bicd1$^{713-802}$) using GFP and Zn-5 antibodies. Scale bars, 25 µm. RoP-like sMN axons overexpressing GFP-bicd1$^{713-802}$ were abnormally split or defasciculated (arrows) compared with GFP-negative axons (asterisk) of the same transgenic embryos or RoP-like sMN axons expressing the GFP alone (empty arrowheads, left-hand panels). **(E and F)** Mean number of defasciculated/split, missing or caudally projecting rostral nerves per 10 GFP-positive and -negative hemisegments of 56-hpf Tg(*HuC*:GAL4; *UAS*:GFP) ($n$ = 13; E) and Tg(*HuC*:GAL4; *UAS*:GFP-bicd1$^{713-802}$) ($n$ = 13; F) transgenic larvae. ***, P ≤ 0.001; ns, non-significant; two-way ANOVA with Bonferroni's post test. Error bars are SEM. The same experiment was reproduced three times independently and gave rise to identical statistical differences.

observed in *dynactin1b*$^{-/-}$ CRISPR/Cas9 mutants (Fig. 8, C–E) and overlapped those observed following Fignl1 overexpression (Fig. 8 F; Fassier et al., 2018), supporting a role for Fignl1 as a negative regulator of the dynein/dynactin complex in navigating motor axons. Consistently, partial inhibition of dynein activity using low doses of Ciliobrevin D (1 µM) reduced by 40% the number of defasciculated/split rostral nerves per Fignl1-depleted larva compared with DMSO treatment (Fig. 8, G and H). This partial rescue demonstrates that dysregulated dynein activity contributes to the sMN pathfinding defects of Fignl1-depleted larvae.

In conclusion, our data suggest that Fignl1 regulates bidirectional axonal transport by limiting dynein-driven motility, as a result of its interaction with the opposite polarity-directed motor Kif1bβ, thereby ensuring motor axon targeting most likely through accurate cargo delivery.

## Discussion

Our study uncovers a novel MT-based function for the ATPase Fignl1 in zebrafish motor axon targeting, in addition to its role in the regulation of MT plus-end dynamics (Fassier et al., 2018).

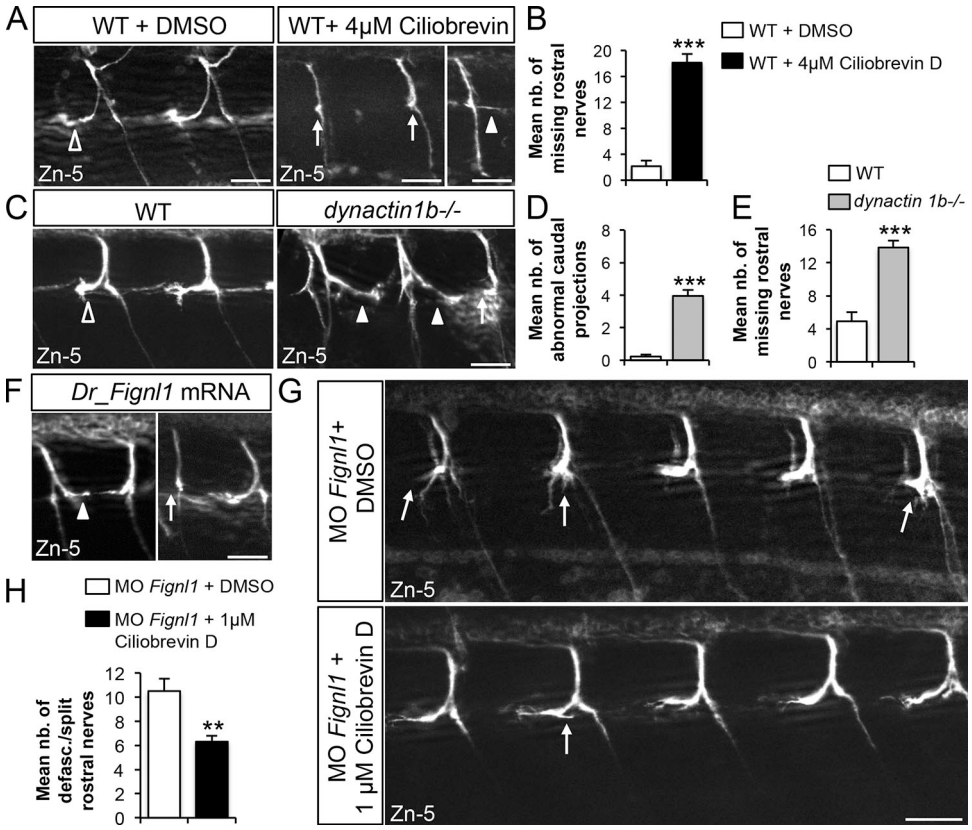


Figure 8. **Fignl1-mediated restriction of dynein activity is required for accurate navigation of RoP-like sMN axons. (A and B)** Immunolabeling of sMN axons in 56-hpf WT larvae treated at 46 hpf with 4 µM of the dynein inhibitor Ciliobrevin D or its vehicle (DMSO) using the Zn-5 antibody. **(B)** Quantification of the mean number of missing rostral nerves in Ciliobrevin- and DMSO-treated WT larvae. **(C)** Immunolabeling of sMN in 56-hpf WT and *dynactin1b*$^{-/-}$ mutant larvae. **(D and E)** Mean number of mistargeted (i.e., caudally oriented; D) or missing (E) rostral nerves in control and mutant larvae. **(F)** Analysis of sMN in 56-hpf control and Fignl1-overexpressing larvae. **(A–F)** Loss of dynein or dynactin 1b function leads to sMN axon pathfinding defects that reproduce those observed in Fignl1-overexpressing embryos. **(G)** Immunolabeling of sMN axons in 56-hpf *Fignl1* morphant larvae treated with 1 µM Ciliobrevin D or DMSO. **(H)** Mean number of defasciculated/split rostral nerves in Ciliobrevin D– or DMSO-treated larvae. Pharmacological reduction of dynein activity partially rescues the axon pathfinding defects of RoP-like sMN axons in Fignl1-depleted larvae. **(A, C, F, and G)** Empty arrowheads indicate normal rostral nerves. Arrowheads and arrows, respectively, point at misguided and missing (A, C, and F) or defasciculated/split (G) rostral nerves. Scale bars, 40 µm. **(B, D, E, and H)** Quantifications were performed in 24 spinal hemisegments of 28 DMSO-treated and 27 Ciliobrevin D–treated control larvae (B), 39 WT and 37 *dynactin1b*$^{-/-}$ mutant larvae (D and E), and 36 DMSO-treated and 36 Ciliobrevin D–treated *Fignl1* morphant larvae (H) pooled from three independent experiments. **, P ≤ 0.01; ***, P ≤ 0.001; ns, nonsignificant; Mann–Whitney test (B, D, E, and H). Error bars are SEM.

Indeed, we here identify Fignl1 as a regulator of bidirectional axonal transport through its coupling with the dynein/dynactin complex via Bicd1 and the opposite polarity-directed motor Kif1bβ. Our analysis further provides in vivo evidence supporting the key role of this tripartite complex in motor axon pathfinding through the restriction of dynein-based transport velocity. Finally, we here report the first direct interaction between a meiotic clade ATPase and a molecular motor in the regulation of axonal transport.

### Meiotic clade ATPases in the regulation of axonal transport: A direct regulation of molecular motor activity by Fignl1

Fignl1 belongs to the meiotic clade of the AAA$^+$ ATPases together with the MT-severing enzymes spastin, katanin, and fidgetin (Roll-Mecak and McNally, 2010; Sharp and Ross, 2012; Monroe and Hill, 2016). These proteins have been involved in a wide variety of MT-related processes and were shown to participate in common cellular functions through distinct molecular mechanisms (Zhang et al., 2007; Yu et al., 2008). In this context, we recently uncovered non-overlapping key roles for the zebrafish orthologue of the hereditary spastic paraplegia protein spastin and its closest homologue Fignl1 in zebrafish motor axon navigation, providing new molecular insight into their functional specificity. While we uncovered spastin long isoform as a bone morphogenetic protein inhibitor required for accurate SMN axon targeting, spastin short isoform was identified as a downstream effector of neuropilin-1 in SMN migration (Jardin et al., 2018). We here report a novel role for Fignl1 in the regulation of bidirectional axonal transport in navigating SMN axons, in addition to its recently discovered role in the regulation of MT plus-end dynamics (Fassier et al., 2018). Indeed, we showed that cooperative interaction between Fignl1, the kinesin Kif1bβ, and the dynein/dynactin adaptor Bicd1 is required for accurate sMN axon pathfinding via the restriction of dynein-based transport. Interestingly, p60-katanin was shown to directly bind the dynein motor and its regulators LIS-1 and NDEL1

(Toyo-Oka et al., 2005). However, while NDEL1-mediated dynein activity at the axon initial segment was shown to be critical for polarized cargo transport (Kuijpers et al., 2016), functional evidence reporting a role for p60-katanin in this process has not been reported. Similarly, although spastin loss of function was shown to impair anterograde and retrograde axonal transport of diverse cargoes, both in vivo and in vitro, no direct molecular link between this MT-severing enzyme and a molecular motor has been identified so far. Spastin-related axonal transport defects were suggested to arise from primary failure in MT organization, dynamics, and post-translational modifications (Tarrade et al., 2006; Kasher et al., 2009; Fassier et al., 2013; Denton et al., 2014; Havlicek et al., 2014; Plaud et al., 2017), or via a MT-independent and toxic effect of few spastin pathogenic mutations that affect molecular motor phosphorylation by casein kinase 2 (Leo et al., 2017). Thus, our analysis reports on the first direct molecular and functional links between a meiotic clade ATPase and two opposite teams of molecular motors in the regulation of bidirectional axonal transport required for neuronal connectivity.

### Fignl1, a new regulator of bidirectional vesicular trafficking via dynein speed restriction

Although multiple adaptor proteins and cofactors linking molecular motors to cargoes are assumed to regulate cargo movement via the modulation of molecular motor activity (Schlager and Hoogenraad, 2009; Akhmanova and Hammer, 2010; Jolly and Gelfand, 2011; Fu and Holzbaur, 2014), the exact identity of all these proteins remains largely unknown. Bicd proteins have been described in this context as key regulators of dynein-mediated retrograde transport velocity (Schlager et al., 2014). We here propose that Fignl1-mediated coupling between Bicd1 and Kif1bβ plays a crucial role in the regulation of dynein-based transport, as suggested in vivo by increased retrograde velocity of Rab3 (a known Kif1bβ cargo; Niwa et al., 2008) vesicles in Fignl1-depleted navigating axons. Furthermore, since Fignl1 depletion also reduced Rab3 vesicular anterograde run lengths, this ATPase appears to participate in the regulation of Kif1bβ processivity or in its coupling to the dynein/dynactin complex for optimal processive motility. Further investigations will be required to determine whether Fignl1-mediated regulation of bidirectional axonal transport could occur via a tug of war or a cooperative process (Hancock, 2014). Notably, such an impact of Fignl1 depletion on Rab3 transport—and more specifically on dynein velocity and Kif1bβ processivity—would not be expected if Fignl1 were a simple Kif1bβ cargo, as recently reported for the MT regulator SCG10 (Drerup et al., 2016). This is also consistent with our data demonstrating that, unlike SCG10, Fignl1 enrichment in the axon distal portion is not affected by *kif1b* mutation. Finally, our work strengthens previous studies reporting a physical (Grigoriev et al., 2007; Schlager et al., 2010) or genetic (Aguirre-Chen et al., 2011) interaction between proteins of the bicd family and different kinesins by showing their physical and functional link in a physiological context of neuronal circuit wiring.

### Fignl1 controls motor axon pathfinding by limiting dynein activity

Neuronal circuit connectivity relies on precise spatial and temporal delivery of specific organelles and vesicles to different neuronal subcellular compartments (Tojima et al., 2007, 2011; Akiyama et al., 2016). In this context, different regulatory and adaptor proteins are emerging as critical to assist opposite teams of molecular motors in their fine-tuned delivery of specific cargoes in developing neurons (Akhmanova and Hammer, 2010; Fu and Holzbaur, 2014; Schlager et al., 2014; Cross and Dodding, 2019; Olenick and Holzbaur, 2019). Although in vitro studies have highlighted the importance of the regulation of cargo transport velocity for axon outgrowth (Schlager et al., 2010, 2014), an in vivo role for such mechanisms in axon navigation processes is still lacking. Using in vivo time-lapse imaging, as well as genetic (i.e., *dynactin1b*, *fignl1*, and *kif1b* mutants and a dominant-negative approach to disrupt the Bicd1/Fignl1 interaction) and pharmacological (i.e., the dynein inhibitor Ciliobrevin D) approaches, we here provide compelling functional evidence supporting (1) a causal relationship between Fignl1-mediated regulation of dynein-based transport and its control of sMN axon navigation—including the Ciliobrevin D–mediated rescue of Fignl1-depleted sMN axon pathfinding defects—and (2) establishing a key role for molecular motor-based axonal transport in axon navigation processes. Notably, we showed that Fignl1 binding to Bicd1 is key for Fignl1/Kif1bβ-directed motor axon pathfinding (Fig. 7), which is strengthened by the restricted expression pattern of *bicd1* compared with *fignl1* and *kif1bβ* profiles (Fig. 7 versus Fig. 2) in this neuronal population. Altogether, our results support a model in which Fignl1 restricts dynein-based transport velocity by promoting the coupling of the dynein/dynactin complex (via Bicd1) with the opposing motor Kif1bβ (Fig. 9) onto a same vesicle, thereby regulating bidirectional axonal transport and the delivery of key cargoes for RoP-like sMN axon targeting (Fig. 9). However, a role for Fignl1 in the initiation phase of dynein–driven retrograde transport (Splinter et al., 2012) in addition to its restriction of dynein velocity cannot be totally excluded, based on its negative influence on dynactin 1 binding at MT plus ends (Fassier et al., 2018). Furthermore, given the overlap between the binding sites for Fignl1 on both Bicd1 and Kif1bβ and their respective binding sites for Rab6 (Matanis et al., 2002) or DENN/MADD (differentially expressed in normal versus neoplastic/MAPK activating death domain; Niwa et al., 2008) and IGFR1 (Xu et al., 2018), Fignl1 could also play a role in the selectivity for transported cargoes through a competition process, as suggested for Hook1 (Olenick et al., 2018).

Finally, regarding the nature of the transported cargo, neurotrophin receptors, which have been implicated in axon pathfinding processes (Marler et al., 2008, 2010; Poopalasundaram et al., 2011), and were shown to be trafficked through kif1bβ- (Tanaka et al., 2016; Fell et al., 2017), dynein- (Olenick et al., 2018), or bicd1-dependent processes (Terenzio et al., 2014), appear as promising candidates. Alternatively, bone morphogenetic protein signaling, which recently emerged as a key guidance pathway in zebrafish RoP-like sMN axon targeting (Jardin et al., 2018) and relies on dynein-based retrograde

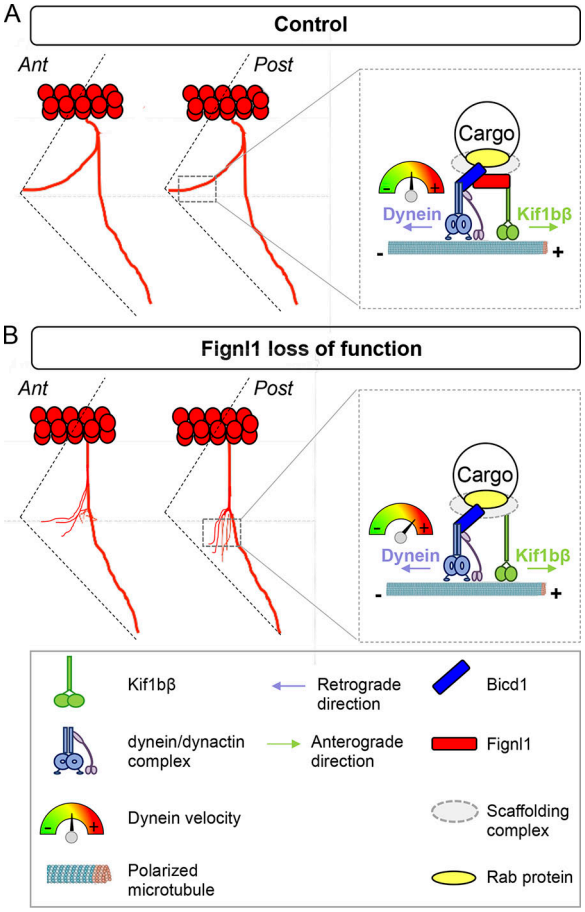


Figure 9. **Hypothetical model of Fignl1-mediated regulation of dynein-based retrograde transport velocity during motor axon pathfinding. (A and B)** Left-hand panels schematize the physiological consequences of Fignl1 loss of function (B) on SMN axon pathfinding compared with normal conditions (A). Schemes represent lateral views of two zebrafish hemisegments, anterior to the left. Ant, anterior; Post, posterior. Boxed right-hand panels focus on the molecular model that might underlie SMN navigational behavior in each condition. **(A)** In healthy conditions, Fignl1 may promote the recruitment of Kif1bβ onto dynein-bound cargoes—or vice versa—which could decrease the velocity of the dynein/dynactin complex through a tug of war or a cooperative mechanism. Fignl1-mediated inhibition of dynein velocity may then regulate the delivery of cargoes required for accurate rostral nerve targeting. **(B)** Fignl1 depletion could reduce the number of dynein-attached cargoes associated with Kif1bβ and would thus increase dynein-mediated retrograde axonal transport velocity, ultimately affecting the distribution of cargoes critical for rostral nerve fasciculation and pathfinding.

transport to regulate synaptic growth at the *Drosophila melanogaster* neuromuscular junction (McCabe et al., 2003; Ball et al., 2010), also comes out as an attractive candidate.

Finally, defective axonal transport of specific cargoes is a major feature of many neurodegenerative disorders (Millecamps and Julien, 2013). Notably, both *KIF1Bβ* and *BICD* loci have been involved in neurodegenerative disorders affecting the motor system (Zhao et al., 2001; Pantelidou et al., 2007; Neveling et al., 2013; Martinez-Carrera and Wirth, 2015). This molecular complex may thus be critical not only for the establishment of motor circuits but also for the maintenance of their homeostasis. Our work may therefore provide new insight into the molecular processes implicated in axonal transport-related disorders.

## Materials and methods

### Yeast two-hybrid screen

The yeast two-hybrid screen was conducted by Hybrigenics. cDNA encoding the N-terminal part of the mouse fignl1 (aa 1–441) was used as bait to screen an E16 mouse embryonic brain cDNA library. A total of three and two independent clones containing *kif1bβ* or *bicd1* cDNA fragments were respectively isolated from this screen.

### Antibodies and plasmid constructs

The following primary antibodies were used in this study: mouse Zn-5 (Zebrafish International Resource Center [ZIRC]; University of Oregon), mouse F310 (Developmental Studies Hybridoma Bank; F310 was deposited to the bank by F.E. Stockdale, Stanford University School of Medicine, Stanford, CA), mouse RMO44 (130500; Invitrogen), rabbit Fignl1 3353 (Fassier et al., 2018), rabbit GFP (A11122; Invitrogen), Alexa Fluor 488–conjugated phalloidin (A12379; Invitrogen), mouse tyrosinated tubulin (T9028; Sigma-Aldrich), rat HA (11867423001; Roche), rabbit Flag (F7425; Sigma-Aldrich), rabbit KIF1B (sc-376246; Santa Cruz Biotechnology), and mouse dynactin 1 (610473; BD Transduction Laboratories).

Mouse and zebrafish constructs of full-length and N-terminally truncated Fignl1 (Dr_Fignl1-HA; Dr_Fignl1Δ1-173-HA) had been generated for previous studies in the laboratory (Fassier et al., 2018).

pEYFP-C1Hu_KIF1Bβ and *UAS*:Rab3-Dendra2 constructs were provided by N. Santama (University of Cyprus, Nicosia, Cyprus; Charalambous et al., 2013) and V. Bercier and F. Del Bene (Institut Curie, Paris, France), respectively. The p14*UAS*:Dr_Fignl1-TRFP and p14*UAS*:YFP-Hu_KIF1Bβ were generated using the NEBuilder HiFi DNA Assembly Cloning kit (NEB) in the pT1UciMP plasmid containing a 14xUAS-E1b promoter and UbC intron with tol1 sites (Horstick et al., 2015) and linearized with NcoI. Dr_Fignl1 cDNA was PCR-amplified from a pCS2+ *FL-Fignl1-HA* vector (Fassier et al., 2018) and fused with an TagRFP-Tag sequence with the GCCGGCGGCGGCGGATCC linker. YFP-Hu_KIF1Bβ was PCR-amplified from the pEYFP-C1Hu_KIF1Bβ vector provided by N. Santama (Charalambous et al., 2013).

Mouse *bicd1* cDNA (NM_009753) was reverse-transcribed, PCR-amplified (forward primer: 5′-ATCCGGAATTCATGGACT ACAAAGACGATGACGACAAGGCCGCAGAGGAGGCGCTGAAGA CG-3′; reverse primer: 5′-CTAGTCTAGACTAGTTGTGAGCAC TGTGGCGGTACGGA-3′) and Flag-tagged using the SuperScript III One-Step RT-PCR System with Platinum Taq High Fidelity (Thermo Fisher Scientific) from a total RNA extract of E16.5 mouse embryonic brain following the manufacturer's instructions. The PCR product was subsequently cloned in the pCS2+ vector using EcoRI and XbaI restriction sites. Mouse *bicd1* cDNA was additionally PCR-amplified (forward primer: 5′-CCG CTCGAGTGGCCGCAGAGGAGGCGCTGAAGACG-3′ and reverse primer: 5′-CGCGGATCCCTAGTTGTGAGCACTGTGGCGGTACGG AGG-3′) and cloned in the pEGFP-C1 vector using the XhoI and

BamHI restriction sites (pEGFP-C1 Ms_bicd1). The bicd1 (683–813), (683–712), (713–802), and (803–813) constructs were PCR-amplified from the pEGFP-C1 Ms_bicd1 construct using the AccuPrime Taq DNA Polymerase System (Thermo Fisher Scientific) and subcloned into the pEGFP-C1 vector using the XhoI and BamHI restriction sites or into the *UAS*_self vector (kindly provided by S. Gerety, D. Wilkinson's laboratory, The Francis Crick Institute, London, UK) using the EcoRI and AvrII restriction sites. The *UAS*_self:EGFP construct was generated and kindly provided by S. Couvet from X. Nicol's laboratory (Institut de la Vision, Paris, France).

All clones were sequenced before use and the plasmids were purified using a QIAfilter EndoFree Plasmid Maxi Kit (QIAGEN).

### Cell culture, transfection, and immunocytochemistry

COS-7 cells were cultured in DMEM supplemented with 10% fetal calf serum at 37°C under 5% $CO_2$. cDNA constructs were transfected using Lipofectamine 2000 according to the manufacturer's instructions (Life Technologies) with a DNA:Lipofectamine ratio of 1:1.5. Cells were fixed 24 h after transfection in ice-cold methanol for 10 min at −20°C and post-fixed with a 4% PFA/4% sucrose solution for 20 min at room temperature. Cells were then blocked in PBS–3% BSA supplemented with 5% normal goat serum and incubated with HA (1/100), GFP (1/1,000), and tyrosinated tubulin (1/4,000) antibodies. After several washes in PBS, cells were incubated with appropriate Alexa Fluor–conjugated secondary antibodies. Images were acquired using an inverted fluorescence microscope equipped with an Apotome module (Axiovert 200M; Zeiss), the AxioCam MRm camera (Zeiss), a 20× objective (NA 0.5), and the Axiovision software (Zeiss). Images were processed with the National Institutes of Health ImageJ software. Figure panels correspond to a projection image from a z-stack of 0.3-µm sections.

### Co-IP assays and Western blot analysis

For co-IP assays, transfected COS-7 cells were lysed in radioimmunoprecipitation assay (RIPA) buffer (50 mM Tris-HCl, pH 7.4, 150 mM NaCl, 20 mM EGTA, 1% NP-40, 0.5% sodium deoxycholate, and 0.1% SDS) supplemented with a cocktail of protease inhibitors (Roche). Co-IPs were performed by incubating 1 mg of precleared protein extracts with 40 µl of GFP-Trap_A (Chromotek) or 20 µl of HA-trap agarose beads (Pierce) for 4 h at 4°C. Immunoprecipitation of endogenous kif1bβ was performed by subsequently incubating 1 mg of precleared protein extract with 4 µg of KIF1B antibody (Sc-376246; Santa Cruz Biotechnology) and 40 µl of Protein G-sepharose (GE Healthcare). Beads were washed several times in RIPA buffer and resuspended in 2X Laemmli buffer. Proteins retained on the beads were then electrophoresed into a 10% SDS-PAGE gel and transferred onto nitrocellulose membranes. Immunoblotting was performed after overnight incubation at 4°C with HA (1/5,000), Flag (1/1,000), GFP (1/8,000), KIF1B (1/1,000), or dynactin 1 (1/2,000) antibodies. Immunostained proteins were visualized using appropriate peroxydase-labeled secondary antibodies (Jackson ImmunoResearch) and the SuperSignal West Pico PLUS Chemiluminescent substrate (Thermo Fisher Scientific).

### Zebrafish lines, care, and maintenance

Zebrafish embryos (*Danio rerio*) were obtained from natural spawning of WT, *kif1b*$^{st43}$ (Lyons et al., 2009), *fignl1*$^{sa22254}$ (Sanger Institute, purchased from the ZIRC), *dynactin1b*$^{-/-}$ mutants, Tg(mnGFF7) (Asakawa et al., 2008, 2013), or Tg (*HuC*:GAL4) (Akerboom et al., 2012) transgenic fish. For CRISPR/Cas9-mediated knock-in of *dynactin1b*, the target site for guide RNA sequences (CCATGTAACGCTCTTTAGCT) was the exon 5 of the *dynactin1b* transcript *dctn1b-202* (ENSDART00000169953.1) and the exon 8 of the *dctn1b-201* transcript (ENSDART00000102411.4). We identified an allele with an insertion of 157 bp leading to a premature stop codon at the position 253 aa of the WT protein. The founder was out-crossed to WT fish, and subsequent generations were in-crossed to generate a homozygous mutant line. The guide RNAs were synthesized using the Megascript T7 transcription kit (Ambion) and purified using the RNAeasy Mini Kit (QIAGEN). The *cas9* mRNA was transcribed using the mMessage mMachine T7 kit (Life Technologies), followed by a DNase-I polyA-tailing reaction.

All embryos were maintained at 28°C in E3 medium and staged by hpf and gross morphology according to Kimmel et al. (1995). Pigment formation was prevented by adding 0.2 mM of 1-phenyl-2-thiourea (Sigma-Aldrich) to the E3 medium past the prim-5 stage. Pharmacological inhibition of the dynein motor was performed by adding either 4 or 1 µM of Ciliobrevin D (Calbiochem) or equivalent volumes of the vehicle (DMSO) to the E3 medium of dechorionated 46-hpf WT or *Fignl1* morphant embryos.

All our experiments were made in agreement with the European Directive 210/63/EU on the protection of animals used for scientific purposes, and the French application decree "Décret 2013–118." The fish facility has been approved by the French "Service for Animal Protection and Health," with the approval number A-75-05-25.

### Genomic DNA isolation and genotyping

Genomic DNA was isolated by incubating larval heads overnight at 55°C in lysis buffer (100 mM Tris HCl, 2 mM EDTA, pH 8, 0.2% Triton X-100, and 250 µg/ml proteinase K). Homozygous *kif1b*$^{st43}$ mutants were identified using established genotyping protocols (Lyons et al., 2009). *Dynactin1b and fignl1*$^{sa22254}$ mutants were respectively identified by PCR amplification of their genomic DNA followed by RsaI digestion or DNA sequencing (GENEWIZ). The following primers were used for PCR: dnct1b_FOR: 5′-CTGCTCCACTGCTTTAAAGGCCAC-3′; dnct1b_ REV: 5′-GTGAGC GAGGCGCTGGCGGACAG-3′; fignl1sa22254_FOR: 5′-GGATGCGCT CTCCCTGTAGATCC-3′; and fignl1sa22254_REV: 5′-AACATTGCC TGGAGAACCTCGTTGG-3′.

### Whole-mount in situ hybridization

The cDNA fragments of *kif1bβ*, *bicd1(K18)* and *bicd1(K4)* were reverse transcribed and PCR amplified using the SuperScript III One-Step RT-PCR System with Platinum Taq High Fidelity (Thermo Fisher Scientific) from total RNA extracts of 24-hpf

zebrafish embryos following the manufacturer's instructions. The following primers were used: zKif1bβ forward: 5′-AATTGTAATACGACTCACTATAGGGAGGAGGATGAAGTGCCCTGG-3′; zKif1bβ reverse: 5′-TCAGAATTAACCCTCACTAAAGGGATAGGTGAGCTCCCAACCAGC-3′; zBicd1(K18) (Ensembl; ENSDART00000112671.3) forward: 5′-AATTGTAATACGACTCACTATAGGGGTTACATTTAGCGAGGAACTTGC-3′; zBicd1(K18) reverse: 5′-TCAGAATTAACCCTCACTAAAGGGAGTTACATACTCATCACATCTTGTTGC-3′; zBicd1(K4) (Ensembl; ENSDART00000168633.1) forward: 5′-AATTGTAATACGACTCACTATAGGGGCATTGGAGACGCATGGAATTCTGG-3′; and zBicd1(K4) reverse: 5′-TCAGAATTAACCCTCACTAAAGGGAGCTCAGGAGAGACTTGAGTTTGAGG-3′. Digoxigenin-labeled *kif1bβ*, *bicd1(K18)*, and *bicd1(K4)* antisense RNA probes were synthesized from purified RT-PCR products using the T3 RNA polymerase (Promega) according to the supplier's instructions. Whole-mount in situ hybridization experiments were performed using standard procedures (Macdonald et al., 1994). Pictures were acquired with a binocular stereomicroscope (Leica M165C) combined with a high definition camera (Leica IC80 HD), then adjusted for brightness and contrast with ImageJ software.

### Morpholinos and RNA injections

Antisense MOs targeting specific splice junctions of *kif1bα* or *kif1bβ* transcripts were kindly provided by D. Lyons (University of Edinburgh, Edinburgh, Scotland; Lyons et al., 2009). The efficiency of these splice site MOs was assessed by RT-PCR from 26-hpf MO *Kif1bα*- or *Kif1bβ*-injected larvae using the SuperScript III One-Step RT-PCR System with Platinum Taq (Thermo Fisher Scientific) and the following primers: RT-PCR 1: *Kif1bα* MO RT-PCR_FOR and *Kif1bα* MO RT-PCR_REV (Lyons et al., 2009); RT-PCR2: *Kif1bα* MO RT-PCRjct_FOR (5′-AGAGATGGAGAAGAGGCTTACAG-3′) and *Kif1bα* MO RT-PCR_REV (Lyons et al., 2009); RT-PCR3: *Kif1bβ* MO RT-PCR_FOR and *Kif1bβ* MO RT-PCR_REV (Lyons et al., 2009); RT-PCR4: *Kif1bβ* MO RT-PCRjct_FOR (5′-CCCTGGAGAAGCTGAAGCAGAGG-3′) and *Kif1bβ* MO RT-PCRjct_REV (5′-TACTCAGGTACACGAAGGCTCTGC-3′).

The universal control MO (5′-CCTCTTACCTCAGTTACAATTTATA-3′) was developed and designed by GeneTools (Philomath).

All MOs were injected at the two-cell stage. MO *Kif1bβ* and MO *Kif1bα* were respectively injected at 1.4 and 0.7 pmol/embryo, while MO *Fignl1* (Fassier et al., 2018) was injected at 0.4 pmol/embryo. For Fignl1 gain-of-function experiments, mRNAs were in vitro transcribed from linearized pCS2+ constructs using the SP6 mMessage mMachine kit (Ambion) and injected at the one-cell stage as previously described (Fassier et al., 2018).

### Whole-mount immunohistochemistry and data analysis

Zebrafish embryos or larvae were fixed in 4% PFA for 2 h at room temperature, washed with 1% Triton X-100 in PBS (PBT1%), permeabilized in a 0.25% trypsin solution (at 25°C) after 24 hpf, blocked for 2 h in PB-T1% supplemented with 10% normal goat serum, and subsequently incubated overnight with Zn-5 (1/200), GFP (1/1,000), and F310 (1/100) antibodies. After several washes in PB-T1%, larvae were incubated overnight at 4°C with Alexa Fluor 488– or 555–conjugated goat anti-mouse antibodies (1/1,000, Molecular Probes) and/or Alexa Fluor 488–conjugated phalloidin (1/100). For RMO44 immunolabeling, larvae were fixed overnight in methanol at −20°C; permeabilized in ice-cold acetone for 5 min at −20°C; blocked 1 h in PBS supplemented with 2% normal goat serum, 1% BSA, 1% DMSO, and 0.1% Triton X-100; and incubated overnight at 4°C with the RMO44 antibody (1/50). Images were acquired using a fluorescence microscope equipped with an Apotome module (Axiovert 200M; Zeiss), a 20× objective (NA 0.5), the AxioCam MRm camera (Zeiss), and the Axiovision software (Zeiss). Images were processed with ImageJ software. Each figure panel corresponds to a projection image from a z-stack of 2-µm sections. The number of rostral nerve defect per embryo was estimated in 12 (for *fignl1*$^{sa22254}$ mutants) or 24 spinal hemisegments located around the yolk tube. At least 18 embryos pooled from three to four independent experiments were analyzed per condition.

For Fignl1 immunolabeling, 26-hpf embryos were fixed for 4 h at 4°C; blocked in PBS supplemented with 5% normal goat serum, 4 mg/ml BSA, and 0.5% Triton X-100; and incubated overnight at 4°C with Fignl1 3353 antibody diluted in the blocking buffer (1/200). Z-stacks of 0.33-µm sections were acquired with the 63× immersion objective (NA 1.4) of the same microscope (i.e., described in the cell culture section) using identical settings (exposure time, z-stack thickness) for control and *kif1b*$^{st43}$ mutant embryos. The fluorescence intensity profile of Fignl1 in the distal portion of SMN axons was estimated along a 15-µm-length lane starting from the GC ($n$ = 35 control axons, and $n$ = 78 *kif1b*$^{st43}$ mutant axons). Fignl1 fluorescence intensity within SMN GCs was estimated with respect to the GC area (ImageJ software). The fluorescence intensity background was measured in an adjacent region of the GC using the same region of interest and was subtracted from each Fignl1 value before statistical analysis. At least 41 GCs from control ($n$ = 9) and *kif1b*$^{st43}$ mutant ($n$ = 13) embryos were analyzed from two independent experiments.

### Touch-evoked escape response test and manual tracking

Locomotor behavior of zebrafish larvae injected with control, *Kif1bβ*, or *Kif1bα* morpholinos was assessed at 56-hpf using the touch-evoked escape response test. A tactile stimulus was applied on each larva with a pair of forceps, and their escape behavior was recorded under a Leica M165 C binocular stereomicroscope equipped with a Leica IC80 HD camera. Swimming speed and covered distance for each larva were quantified using the Manual Tracking plugin (ImageJ software). At least 45 larvae from three independent experiments were analyzed per condition.

### In vivo time-lapse recording of Rab3 vesicles and data analysis

For Rab3-Dendra2 transport analysis, Tg(mnGFF7) transgenic embryos were injected at the one-cell stage with a solution containing 25 ng/µl of a Tol2 *UAS*:Rab3-Dendra2 plasmid and 25 ng/µl of Tol2 transposase mRNAs. Embryos were subsequently injected at the two-cell stage with control, *Kif1bβ*, or *Fignl1* morpholinos. For Fignl1-TRFP transport analysis, Tg(*HuC*:GAL4) transgenic embryos were injected at the one-cell stage with a

solution containing 30 ng/µl of a Tol1 *UAS14*:Fignl1-TRFP plasmid and 30 ng/µl of Tol1 transposase mRNAs. In vivo colocalization analysis between Fignl1 and KIF1Bβ was performed by injecting one-cell stage Tg(*HuC*:GAL4) transgenic embryos with a solution containing 15 ng/µl of a Tol1 *UAS14*:Fignl1-TRFP, 35 ng/µl of Tol1 *UAS14*:YFP-Hu_KIF1Bβ, and 50 ng/µl of Tol1 transposase mRNAs.

For all experiments, injected larvae were screened and sorted at 48 hpf for mosaic expression of the transgenes in SMN using a Macroscope Axio Zoom V 16 (Carl Zeiss). Selected larvae were anesthetized at 50 hpf with tricaine and embedded in 0.8% low melting agarose in a 35-mm glass dish (Ibidi). Time-lapse recordings of Rab3-Dendra2 or Fignl1-TRFP vesicles were acquired at 28°C in E3 medium (supplemented with tricaine) using a Leica DMI 6000B inverted spinning-disk microscope with a 63× immersion objective (NA 1.4) and a 491-nm 100-mW Cobolt calypso laser. Z-stacks of 4.8-µm thickness were acquired every 4 s over a 5-min period with a step size of 0.8 µm using an EMCCD camera (Photometrics Quantem 512 SC) and the Metamorph software (Molecular Devices), and combined into time-lapse movies. Quantifications of Rab3-Dendra2 vesicle velocity and run length were performed in 20 individual sMN axons per genotype, monitored in at least 10 Tg(mnGFF7) transgenic larvae injected with control, *Kif1bβ*, or *Fignl1* morpholinos. Quantifications of both anterograde and retrograde velocities of Fignl1-TRFP–positive vesicles were performed in six individual sMN axons from four different Tg(*HuC*:GAL4; 14*UAS*:Fign1-TRFP) transgenic larvae. Both Rab3-Dendra2 and Fignl1-TRFP motility parameters were analyzed on axonal segments from maximum z-projection movies, using the KymographClear 2.0 macro toolset (Fiji software; Mangeol et al., 2016) to generate kymograms. Slopes and covered distance between two pauses were extracted from segmental manual traces ($n$ = 20–50) on each kymogram and used to determine the mean axonal velocities and run lengths, respectively. Average values obtained for each individual axon were used for statistical analysis. The mean number of Rab3-Dendra2 static particles was determined by counting the number of vertical lines per kymogram, normalized to the length of the imaged axonal segment and the imaging time.

### Statistical analysis

All data were obtained from at least three independent experiments and are presented as mean ± SEM. Statistical significance of the data was evaluated using the parametric unpaired two-tailed $t$ test or the nonparametric Mann–Whitney test when comparing two groups assuming Gaussian or non-Gaussian distributions, respectively. The Kruskal–Wallis ANOVA test with Dunn's post-test or the one-way ANOVA test with Bonferroni's post-test were used when comparing more than two groups assuming non-Gaussian or Gaussian distribution, respectively. Statistical analysis of sMN defects in GFP-positive or -negative hemisegments of Tg(*HuC*:GAL4; *UAS*:GFP) and Tg(*HuC*:GAL4; *UAS*:GFP-bicd1$^{713\text{-}802}$) was performed using the two-way ANOVA test. Data distribution was tested for normality using the D'Agostino and Pearson omnibus normality test. All statistical analyses were performed using Prism 5.0 (GraphPad Software).

### Online supplemental material

Fig. S1 shows that pMN axons of *kif1b*$^{st43}$ mutants develop normally, unlike sMN axons (described in Fig. 2), which fail to navigate properly in a normal muscle environment. Fig. S2 shows *Kif1bα* and *Kif1bβ* knockdown strategy and efficiency. Fig. S3 shows *Kif1bβ* morphant locomotor behavior, muscle fiber development, and reticulospinal axon pathfinding. Video 1 shows Fignl1-TRFP bidirectional axonal transport in navigating sMN axons of 56-hpf transgenic larvae.

## Acknowledgments

We thank the Hybrigenics staff for the yeast two-hybrid screen. We are indebted to David Lyons and Marion Baraban (University of Edinburgh, Edinburgh, Scotland) for providing us with the *kif1b*$^{st43}$ mutant line and genotyping advice as well as the *Kif1bα* and *Kif1bβ* splice site morpholinos. We also thank Giannis Maimaris from Niovi Santama's laboratory and Sebastien Gerety from David Wilkinson's laboratory for providing us with the YFP-Hu_KIF1Bβ and UAS_self constructs. We are obliged to Jean-François Gilles, France Lam, and Susanne Bolte from the imaging facility of the Institut de Biologie Paris-Seine (IBPS; Sorbonne University, Paris, France) for their assistance in microscopy, and Alex Bois, Stéphane Tronche, and Abdelkarim Mannioui from the IBPS aquatic animal facility for fish care. We are grateful to X. Nicol and A. Andrieux for insightful comments on M. Atkins' PhD project or present manuscript.

This work was supported by research grants from the Association Française contre les Myopathies and the Emergence program from the Pierre and Marie Curie University attributed to J. Hazan, the Association Strümpell-Lorrain/Hereditary Spastic Paraplegia France and the Institut National de la Santé et de la Recherche Médicale integration grants attributed to C. Fassier, and the PhD fellowship from the French Ministry of Higher Education, Scientific Research and Training attributed to M. Atkins.

The authors declare no competing financial interests.

Author contributions: C. Fassier conceived the project in J. Hazan's laboratory. C. Fassier, M. Atkins, and L. Gasmi designed the experiments and analyzed the data with J. Hazan. M. Atkins, C. Fassier, and L. Gasmi performed the experiments. V. Bercier, C. Revenu, and F. Del Bene provided the *UAS*:Rab3-Dendra2, 14*UAS*:Fignl1-TRFP, and 14*UAS*:YFP-Hu_KIF1Bβ constructs; created the *dynactin1b* mutant line; and had insightful comments on the project and the manuscript. M. Atkins and C. Fassier wrote the manuscript with the editing of J. Hazan.

Submitted: 23 May 2018
Revised: 30 May 2019
Accepted: 29 July 2019

## References

Aguirre-Chen, C., H.E. Bülow, and Z. Kaprielian. 2011. C. elegans bicd-1, homolog of the Drosophila dynein accessory factor Bicaudal D, regulates the branching of PVD sensory neuron dendrites. *Development.* 138: 507–518. https://doi.org/10.1242/dev.060939

Akerboom, J., T.W. Chen, T.J. Wardill, L. Tian, J.S. Marvin, S. Mutlu, N.C. Calderón, F. Esposti, B.G. Borghuis, X.R. Sun, et al. 2012. Optimization of a GCaMP calcium indicator for neural activity imaging. *J. Neurosci.* 32: 13819–13840. https://doi.org/10.1523/JNEUROSCI.2601-12.2012

Akhmanova, A., and J.A. Hammer III. 2010. Linking molecular motors to membrane cargo. *Curr. Opin. Cell Biol.* 22:479–487. https://doi.org/10.1016/j.ceb.2010.04.008

Akiyama, H., T. Fukuda, T. Tojima, V.O. Nikolaev, and H. Kamiguchi. 2016. Cyclic Nucleotide Control of Microtubule Dynamics for Axon Guidance. *J. Neurosci.* 36:5636–5649. https://doi.org/10.1523/JNEUROSCI.3596-15.2016

Asakawa, K., M.L. Suster, K. Mizusawa, S. Nagayoshi, T. Kotani, A. Urasaki, Y. Kishimoto, M. Hibi, and K. Kawakami. 2008. Genetic dissection of neural circuits by Tol2 transposon-mediated Gal4 gene and enhancer trapping in zebrafish. *Proc. Natl. Acad. Sci. USA.* 105:1255–1260. https://doi.org/10.1073/pnas.0704963105

Asakawa, K., G. Abe, and K. Kawakami. 2013. Cellular dissection of the spinal cord motor column by BAC transgenesis and gene trapping in zebrafish. *Front. Neural Circuits.* 7:100. https://doi.org/10.3389/fncir.2013.00100

Ascaño, M., A. Richmond, P. Borden, and R. Kuruvilla. 2009. Axonal targeting of Trk receptors via transcytosis regulates sensitivity to neurotrophin responses. *J. Neurosci.* 29:11674–11685. https://doi.org/10.1523/JNEUROSCI.1542-09.2009

Ball, R.W., M. Warren-Paquin, K. Tsurudome, E.H. Liao, F. Elazzouzi, C. Cavanagh, B.-S. An, T.-T. Wang, J.H. White, and A.P. Haghighi. 2010. Retrograde BMP signaling controls synaptic growth at the NMJ by regulating trio expression in motor neurons. *Neuron.* 66:536–549. https://doi.org/10.1016/j.neuron.2010.04.011

Cammarata, G.M., E.A. Bearce, and L.A. Lowery. 2016. Cytoskeletal social networking in the growth cone: How +TIPs mediate microtubule-actin cross-linking to drive axon outgrowth and guidance. *Cytoskeleton (Hoboken).* 73:461–476. https://doi.org/10.1002/cm.21272

Charalambous, D.C., E. Pasciuto, V. Mercaldo, P. Pilo Boyl, S. Munck, C. Bagni, and N. Santama. 2013. KIF1Bβ transports dendritically localized mRNPs in neurons and is recruited to synapses in an activity-dependent manner. *Cell. Mol. Life Sci.* 70:335–356. https://doi.org/10.1007/s00018-012-1108-0

Cross, J.A., and M.P. Dodding. 2019. Motor-cargo adaptors at the organelle-cytoskeleton interface. *Curr. Opin. Cell Biol.* 59:16–23. https://doi.org/10.1016/j.ceb.2019.02.010

Deng, C.-Y., W.-L. Lei, X.-H. Xu, X.-C. Ju, Y. Liu, and Z.-G. Luo. 2014. JIP1 mediates anterograde transport of Rab10 cargos during neuronal polarization. *J. Neurosci.* 34:1710–1723. https://doi.org/10.1523/JNEUROSCI.4496-13.2014

Dent, E.W., S.L. Gupton, and F.B. Gertler. 2011. The growth cone cytoskeleton in axon outgrowth and guidance. *Cold Spring Harb. Perspect. Biol.* 3:a001800. https://doi.org/10.1101/cshperspect.a001800

Denton, K.R., L. Lei, J. Grenier, V. Rodionov, C. Blackstone, and X.-J. Li. 2014. Loss of spastin function results in disease-specific axonal defects in human pluripotent stem cell-based models of hereditary spastic paraplegia. *Stem Cells.* 32:414–423. https://doi.org/10.1002/stem.1569

Deppmann, C.D., S. Mihalas, N. Sharma, B.E. Lonze, E. Niebur, and D.D. Ginty. 2008. A model for neuronal competition during development. *Science.* 320:369–373. https://doi.org/10.1126/science.1152677

Drerup, C.M., S. Lusk, and A. Nechiporuk. 2016. Kif1B Interacts with KBP to Promote Axon Elongation by Localizing a Microtubule Regulator to Growth Cones. *J. Neurosci.* 36:7014–7026. https://doi.org/10.1523/JNEUROSCI.0054-16.2016

Fassier, C., A. Tarrade, L. Peris, S. Courageot, P. Mailly, C. Dalard, S. Delga, N. Roblot, J. Lefèvre, D. Job, et al. 2013. Microtubule-targeting drugs rescue axonal swellings in cortical neurons from spastin knockout mice. *Dis. Model. Mech.* 6:72–83. https://doi.org/10.1242/dmm.008946

Fassier, C., A. Fréal, L. Gasmi, C. Delphin, D. Ten Martin, S. De Gois, M. Tambalo, C. Bosc, P. Mailly, C. Revenu, et al. 2018. Motor axon navigation relies on Fidgetin-like 1-driven microtubule plus end dynamics. *J. Cell Biol.* 217:1719–1738. https://doi.org/10.1083/jcb.201604108

Fell, S.M., S. Li, K. Wallis, A. Kock, O. Surova, V. Rraklli, C.S. Höfig, W. Li, J. Mittag, M.A. Henriksson, et al. 2017. Neuroblast differentiation during development and in neuroblastoma requires KIF1Bβ-mediated transport of TRKA. *Genes Dev.* 31:1036–1053. https://doi.org/10.1101/gad.297077.117

Fu, M.M., and E.L.F. Holzbaur. 2014. Integrated regulation of motor-driven organelle transport by scaffolding proteins. *Trends Cell Biol.* 24:564–574. https://doi.org/10.1016/j.tcb.2014.05.002

Grabham, P.W., G.E. Seale, M. Bennecib, D.J. Goldberg, and R.B. Vallee. 2007. Cytoplasmic dynein and LIS1 are required for microtubule advance during growth cone remodeling and fast axonal outgrowth. *J. Neurosci.* 27:5823–5834. https://doi.org/10.1523/JNEUROSCI.1135-07.2007

Grigoriev, I., D. Splinter, N. Keijzer, P.S. Wulf, J. Demmers, T. Ohtsuka, M. Modesti, I.V. Maly, F. Grosveld, C.C. Hoogenraad, and A. Akhmanova. 2007. Rab6 regulates transport and targeting of exocytotic carriers. *Dev. Cell.* 13:305–314. https://doi.org/10.1016/j.devcel.2007.06.010

Hancock, W.O. 2014. Bidirectional cargo transport: moving beyond tug of war. *Nat. Rev. Mol. Cell Biol.* 15:615–628. https://doi.org/10.1038/nrm3853

Havlicek, S., Z. Kohl, H.K. Mishra, I. Prots, E. Eberhardt, N. Denguir, H. Wend, S. Plötz, L. Boyer, M.C.N. Marchetto, et al. 2014. Gene dosage-dependent rescue of HSP neurite defects in SPG4 patients' neurons. *Hum. Mol. Genet.* 23:2527–2541. https://doi.org/10.1093/hmg/ddt644

Hines, J.H., M. Abu-Rub, and J.R. Henley. 2010. Asymmetric endocytosis and remodeling of beta1-integrin adhesions during growth cone chemorepulsion by MAG. *Nat. Neurosci.* 13:829–837. https://doi.org/10.1038/nn.2554

Hirokawa, N., S. Niwa, and Y. Tanaka. 2010. Molecular motors in neurons: transport mechanisms and roles in brain function, development, and disease. *Neuron.* 68:610–638. https://doi.org/10.1016/j.neuron.2010.09.039

Hoogenraad, C.C., and A. Akhmanova. 2016. Bicaudal D Family of Motor Adaptors: Linking Dynein Motility to Cargo Binding. *Trends Cell Biol.* 26:327–340. https://doi.org/10.1016/j.tcb.2016.01.001

Horstick, E.J., D.C. Jordan, S.A. Bergeron, K.M. Tabor, M. Serpe, B. Feldman, and H.A. Burgess. 2015. Increased functional protein expression using nucleotide sequence features enriched in highly expressed genes in zebrafish. *Nucleic Acids Res.* 43:e48. https://doi.org/10.1093/nar/gkv035

Itofusa, R., and H. Kamiguchi. 2011. Polarizing membrane dynamics and adhesion for growth cone navigation. *Mol. Cell. Neurosci.* 48:332–338. https://doi.org/10.1016/j.mcn.2011.03.007

Jardin, N., F. Giudicelli, D. Ten Martín, A. Vitrac, S. De Gois, R. Allison, C. Houart, E. Reid, J. Hazan, and C. Fassier. 2018. BMP- and neuropilin 1-mediated motor axon navigation relies on spastin alternative translation. *Development.* 145:dev162701. https://doi.org/10.1242/dev.162701

Jha, R., J. Roostalu, N.I. Cade, M. Trokter, and T. Surrey. 2017. Combinatorial regulation of the balance between dynein microtubule end accumulation and initiation of directed motility. *EMBO J.* 36:3387–3404. https://doi.org/10.15252/embj.201797077

Jolly, A.L., and V.I. Gelfand. 2011. Bidirectional intracellular transport: utility and mechanism. *Biochem. Soc. Trans.* 39:1126–1130. https://doi.org/10.1042/BST0391126

Kahn, O.I., and P.W. Baas. 2016. Microtubules and Growth Cones: Motors Drive the Turn. *Trends Neurosci.* 39:433–440. https://doi.org/10.1016/j.tins.2016.04.009

Kapitein, L.C., and C.C. Hoogenraad. 2011. Which way to go? Cytoskeletal organization and polarized transport in neurons. *Mol. Cell. Neurosci.* 46:9–20. https://doi.org/10.1016/j.mcn.2010.08.015

Kasher, P.R., K.J. De Vos, S.B. Wharton, C. Manser, E.J. Bennett, M. Bingley, J.D. Wood, R. Milner, C.J. McDermott, C.C.J. Miller, et al. 2009. Direct evidence for axonal transport defects in a novel mouse model of mutant spastin-induced hereditary spastic paraplegia (HSP) and human HSP patients. *J. Neurochem.* 110:34–44. https://doi.org/10.1111/j.1471-4159.2009.06104.x

Kimmel, C.B., W.W. Ballard, S.R. Kimmel, B. Ullmann, and T.F. Schilling. 1995. Stages of embryonic development of the zebrafish. *Dev. Dyn.* 203:253–310. https://doi.org/10.1002/aja.1002030302

Kuijpers, M., D. van de Willige, A. Freal, A. Chazeau, M.A. Franker, J. Hofenk, R.J.C. Rodrigues, L.C. Kapitein, A. Akhmanova, D. Jaarsma, and C.C. Hoogenraad. 2016. Dynein Regulator NDEL1 Controls Polarized Cargo Transport at the Axon Initial Segment. *Neuron.* 89:461–471. https://doi.org/10.1016/j.neuron.2016.01.022

Leo, L., C. Weissmann, M. Burns, M. Kang, Y. Song, L. Qiang, S.T. Brady, P.W. Baas, and G. Morfini. 2017. Mutant spastin proteins promote deficits in axonal transport through an isoform-specific mechanism involving casein kinase 2 activation. *Hum. Mol. Genet.* 26:2321–2334. https://doi.org/10.1093/hmg/ddx125

Lorenzo, D.N., A. Badea, J. Davis, J. Hostettler, J. He, G. Zhong, X. Zhuang, and V. Bennett. 2014. A PIK3C3-ankyrin-B-dynactin pathway promotes axonal growth and multiorganelle transport. *J. Cell Biol.* 207:735–752. https://doi.org/10.1083/jcb.201407063

Lyons, D.A., S.G. Naylor, A. Scholze, and W.S. Talbot. 2009. Kif1b is essential for mRNA localization in oligodendrocytes and development of myelinated axons. *Nat. Genet.* 41:854–858. https://doi.org/10.1038/ng.376

Macdonald, R., Q. Xu, K.A. Barth, I. Mikkola, N. Holder, A. Fjose, S. Krauss, and S.W. Wilson. 1994. Regulatory gene expression boundaries demarcate sites of neuronal differentiation in the embryonic zebrafish forebrain. *Neuron.* 13:1039–1053. https://doi.org/10.1016/0896-6273(94)90044-2

Maday, S., A.E. Twelvetrees, A.J. Moughamian, and E.L.F. Holzbaur. 2014. Axonal transport: cargo-specific mechanisms of motility and regulation. *Neuron.* 84:292–309. https://doi.org/10.1016/j.neuron.2014.10.019

Mangeol, P., B. Prevo, and E.J.G. Peterman. 2016. KymographClear and KymographDirect: two tools for the automated quantitative analysis of molecular and cellular dynamics using kymographs. *Mol. Biol. Cell.* 27:1948–1957. https://doi.org/10.1091/mbc.e15-06-0404

Marler, K.J.M., E. Becker-Barroso, A. Martínez, M. Llovera, C. Wentzel, S. Poopalasundaram, R. Hindges, E. Soriano, J. Comella, and U. Drescher. 2008. A TrkB/EphrinA interaction controls retinal axon branching and synaptogenesis. *J. Neurosci.* 28:12700–12712. https://doi.org/10.1523/JNEUROSCI.1915-08.2008

Marler, K.J., S. Poopalasundaram, E.R. Broom, C. Wentzel, and U. Drescher. 2010. Pro-neurotrophins secreted from retinal ganglion cell axons are necessary for ephrinA-p75NTR-mediated axon guidance. *Neural Dev.* 5: 30. https://doi.org/10.1186/1749-8104-5-30

Martinez-Carrera, L.A., and B. Wirth. 2015. Dominant spinal muscular atrophy is caused by mutations in BICD2, an important golgin protein. *Front. Neurosci.* 9:401. https://doi.org/10.3389/fnins.2015.00401

Matanis, T., A. Akhmanova, P. Wulf, E. Del Nery, T. Weide, T. Stepanova, N. Galjart, F. Grosveld, B. Goud, C.I. De Zeeuw, et al. 2002. Bicaudal-D regulates COPI-independent Golgi-ER transport by recruiting the dynein-dynactin motor complex. *Nat. Cell Biol.* 4:986–992. https://doi.org/10.1038/ncb891

McCabe, B.D., G. Marqués, A.P. Haghighi, R.D. Fetter, M.L. Crotty, T.E. Haerry, C.S. Goodman, and M.B. O'Connor. 2003. The BMP homolog Gbb provides a retrograde signal that regulates synaptic growth at the Drosophila neuromuscular junction. *Neuron.* 39:241–254. https://doi.org/10.1016/S0896-6273(03)00426-4

Millecamps, S., and J.-P. Julien. 2013. Axonal transport deficits and neurodegenerative diseases. *Nat. Rev. Neurosci.* 14:161–176. https://doi.org/10.1038/nrn3380

Monroe, N., and C.P. Hill. 2016. Meiotic Clade AAA ATPases: Protein Polymer Disassembly Machines. *J. Mol. Biol.* 428(9, 9 Pt B):1897–1911. https://doi.org/10.1016/j.jmb.2015.11.004

Myers, K.A., I. Tint, C.V. Nadar, Y. He, M.M. Black, and P.W. Baas. 2006. Antagonistic forces generated by cytoplasmic dynein and myosin-II during growth cone turning and axonal retraction. *Traffic.* 7: 1333–1351. https://doi.org/10.1111/j.1600-0854.2006.00476.x

Nadar, V.C., A. Ketschek, K.A. Myers, G. Gallo, and P.W. Baas. 2008. Kinesin-5 is essential for growth-cone turning. *Curr. Biol.* 18:1972–1977. https://doi.org/10.1016/j.cub.2008.11.021

Nadar, V.C., S. Lin, and P.W. Baas. 2012. Microtubule redistribution in growth cones elicited by focal inactivation of kinesin-5. *J. Neurosci.* 32: 5783–5794. https://doi.org/10.1523/JNEUROSCI.0144-12.2012

Neveling, K., L.A. Martinez-Carrera, I. Hölker, A. Heister, A. Verrips, S.M. Hosseini-Barkooie, C. Gilissen, S. Vermeer, M. Pennings, R. Meijer, et al. 2013. Mutations in BICD2, which encodes a golgin and important motor adaptor, cause congenital autosomal-dominant spinal muscular atrophy. *Am. J. Hum. Genet.* 92:946–954. https://doi.org/10.1016/j.ajhg.2013.04.011

Niwa, S., Y. Tanaka, and N. Hirokawa. 2008. KIF1Bbeta- and KIF1A-mediated axonal transport of presynaptic regulator Rab3 occurs in a GTP-dependent manner through DENN/MADD. *Nat. Cell Biol.* 10:1269–1279. https://doi.org/10.1038/ncb1785

O'Donnell, M., R.K. Chance, and G.J. Bashaw. 2009. Axon growth and guidance: receptor regulation and signal transduction. *Annu. Rev. Neurosci.* 32:383–412. https://doi.org/10.1146/annurev.neuro.051508.135614

Olenick, M.A., and E.L.F. Holzbaur. 2019. Dynein activators and adaptors at a glance. *J. Cell Sci.* 132:jcs227132. https://doi.org/10.1242/jcs.227132

Olenick, M.A., R. Dominguez, and E.L.F. Holzbaur. 2018. Dynein activator Hook1 is required for trafficking of BDNF-signaling endosomes in neurons. *J. Cell Biol.* https://doi.org/10.1083/jcb.201805016

Pantelidou, M., S.E. Zographos, C.W. Lederer, T. Kyriakides, M.W. Pfaffl, and N. Santama. 2007. Differential expression of molecular motors in the motor cortex of sporadic ALS. *Neurobiol. Dis.* 26:577–589. https://doi.org/10.1016/j.nbd.2007.02.005

Patel, S., and M. Latterich. 1998. The AAA team: related ATPases with diverse functions. *Trends Cell Biol.* 8:65–71. https://doi.org/10.1016/S0962-8924(97)01212-9

Phillis, R., D. Statton, P. Caruccio, and R.K. Murphey. 1996. Mutations in the 8 kDa dynein light chain gene disrupt sensory axon projections in the Drosophila imaginal CNS. *Development.* 122:2955–2963.

Plaud, C., V. Joshi, M. Marinello, D. Pastré, T. Galli, P.A. Curmi, and A. Burgo. 2017. Spastin regulates VAMP7-containing vesicles trafficking in cortical neurons. *Biochim. Biophys. Acta Mol. Basis Dis.* 1863:1666–1677. https://doi.org/10.1016/j.bbadis.2017.04.007

Poopalasundaram, S., K.J.M. Marler, and U. Drescher. 2011. EphrinA6 on chick retinal axons is a key component for p75(NTR)-dependent axon repulsion and TrkB-dependent axon branching. *Mol. Cell. Neurosci.* 47: 131–136. https://doi.org/10.1016/j.mcn.2011.03.008

Roll-Mecak, A., and F.J. McNally. 2010. Microtubule-severing enzymes. *Curr. Opin. Cell Biol.* 22:96–103. https://doi.org/10.1016/j.ceb.2009.11.001

Schlager, M.A., and C.C. Hoogenraad. 2009. Basic mechanisms for recognition and transport of synaptic cargos. *Mol. Brain.* 2:25. https://doi.org/10.1186/1756-6606-2-25

Schlager, M.A., L.C. Kapitein, I. Grigoriev, G.M. Burzynski, P.S. Wulf, N. Keijzer, E. de Graaff, M. Fukuda, I.T. Shepherd, A. Akhmanova, and C.C. Hoogenraad. 2010. Pericentrosomal targeting of Rab6 secretory vesicles by Bicaudal-D-related protein 1 (BICDR-1) regulates neuritogenesis. *EMBO J.* 29:1637–1651. https://doi.org/10.1038/emboj.2010.51

Schlager, M.A., A. Serra-Marques, I. Grigoriev, L.F. Gumy, M. Esteves da Silva, P.S. Wulf, A. Akhmanova, and C.C. Hoogenraad. 2014. Bicaudal d family adaptor proteins control the velocity of Dynein-based movements. *Cell Reports.* 8:1248–1256. https://doi.org/10.1016/j.celrep.2014.07.052

Sharp, D.J., and J.L. Ross. 2012. Microtubule-severing enzymes at the cutting edge. *J. Cell Sci.* 125:2561–2569. https://doi.org/10.1242/jcs.101139

Splinter, D., D.S. Razafsky, M.A. Schlager, A. Serra-Marques, I. Grigoriev, J. Demmers, N. Keijzer, K. Jiang, I. Poser, A.A. Hyman, et al. 2012. BICD2, dynactin, and LIS1 cooperate in regulating dynein recruitment to cellular structures. *Mol. Biol. Cell.* 23:4226–4241. https://doi.org/10.1091/mbc.e12-03-0210

Steketee, M.B., and J.L. Goldberg. 2012. Signaling endosomes and growth cone motility in axon regeneration. *Int. Rev. Neurobiol.* 106:35–73. https://doi.org/10.1016/B978-0-12-407178-0.00003-X

Tanaka, Y., S. Niwa, M. Dong, A. Farkhondeh, L. Wang, R. Zhou, and N. Hirokawa. 2016. The Molecular Motor KIF1A Transports the TrkA Neurotrophin Receptor and Is Essential for Sensory Neuron Survival and Function. *Neuron.* 90:1215–1229. https://doi.org/10.1016/j.neuron.2016.05.002

Tarrade, A., C. Fassier, S. Courageot, D. Charvin, J. Vitte, L. Peris, A. Thorel, E. Mouisel, N. Fonknechten, N. Roblot, et al. 2006. A mutation of spastin is responsible for swellings and impairment of transport in a region of axon characterized by changes in microtubule composition. *Hum. Mol. Genet.* 15:3544–3558. https://doi.org/10.1093/hmg/ddl431

Terenzio, M., M. Golding, M.R.G. Russell, K.B. Wicher, I. Rosewell, B. Spencer-Dene, D. Ish-Horowicz, and G. Schiavo. 2014. Bicaudal-D1 regulates the intracellular sorting and signalling of neurotrophin receptors. *EMBO J.* 33:1582–1598. https://doi.org/10.15252/embj.201387579

Tischfield, M.A., H.N. Baris, C. Wu, G. Rudolph, L. Van Maldergem, W. He, W.-M. Chan, C. Andrews, J.L. Demer, R.L. Robertson, et al. 2010. Human TUBB3 mutations perturb microtubule dynamics, kinesin interactions, and axon guidance. *Cell.* 140:74–87. https://doi.org/10.1016/j.cell.2009.12.011

Tojima, T., H. Akiyama, R. Itofusa, Y. Li, H. Katayama, A. Miyawaki, and H. Kamiguchi. 2007. Attractive axon guidance involves asymmetric membrane transport and exocytosis in the growth cone. *Nat. Neurosci.* 10:58–66. https://doi.org/10.1038/nn1814

Tojima, T., R. Itofusa, and H. Kamiguchi. 2010. Asymmetric clathrin-mediated endocytosis drives repulsive growth cone guidance. *Neuron.* 66:370–377. https://doi.org/10.1016/j.neuron.2010.04.007

Tojima, T., J.H. Hines, J.R. Henley, and H. Kamiguchi. 2011. Second messengers and membrane trafficking direct and organize growth cone steering. *Nat. Rev. Neurosci.* 12:191–203. https://doi.org/10.1038/nrn2996

Toyo-Oka, K., S. Sasaki, Y. Yano, D. Mori, T. Kobayashi, Y.Y. Toyoshima, S.M. Tokuoka, S. Ishii, T. Shimizu, M. Muramatsu, et al. 2005. Recruitment of katanin p60 by phosphorylated NDEL1, an LIS1 interacting protein, is essential for mitotic cell division and neuronal migration. *Hum. Mol. Genet.* 14:3113–3128. https://doi.org/10.1093/hmg/ddi339

van Spronsen, M., M. Mikhaylova, J. Lipka, M.A. Schlager, D.J. van den Heuvel, M. Kuijpers, P.S. Wulf, N. Keijzer, J. Demmers, L.C. Kapitein, et al. 2013. TRAK/Milton motor-adaptor proteins steer mitochondrial trafficking to axons and dendrites. *Neuron.* 77:485–502. https://doi.org/10.1016/j.neuron.2012.11.027

Xu, F., H. Takahashi, Y. Tanaka, S. Ichinose, S. Niwa, M.P. Wicklund, and N. Hirokawa. 2018. KIF1Bβ mutations detected in hereditary neuropathy impair IGF1R transport and axon growth. *J. Cell Biol.* 217:3480–3496. https://doi.org/10.1083/jcb.201801085

Yu, W., L. Qiang, J.M. Solowska, A. Karabay, S. Korulu, and P.W. Baas. 2008. The microtubule-severing proteins spastin and katanin participate differently in the formation of axonal branches. *Mol. Biol. Cell.* 19: 1485–1498. https://doi.org/10.1091/mbc.e07-09-0878

Zhang, D., G.C. Rogers, D.W. Buster, and D.J. Sharp. 2007. Three microtubule severing enzymes contribute to the "Pacman-flux" machinery that moves chromosomes. *J. Cell Biol.* 177:231–242. https://doi.org/10.1083/jcb.200612011

Zhao, C., J. Takita, Y. Tanaka, M. Setou, T. Nakagawa, S. Takeda, H.W. Yang, S. Terada, T. Nakata, Y. Takei, et al. 2001. Charcot-Marie-Tooth disease type 2A caused by mutation in a microtubule motor KIF1Bbeta. *Cell.* 105: 587–597. https://doi.org/10.1016/S0092-8674(01)00363-4